A viscoelastic two-phase solver using a phase-field approach

Konstantinos Zografos[a,*], Alexandre M. Afonso[b], Robert J. Poole[a], Mónica S. N. Oliveira[c]

[a]*School of Engineering, University of Liverpool, Brownlow Street, Liverpool L69 3GH, UK*
[b]*Centro de Estudos de Fenómenos de Transporte, Departamento de Engenharia Mecânica, Faculdade de Engenharia da Universidade do Porto, 4200-465 Porto, Portugal*
[c]*James Weir Fluids Laboratory, Department of Mechanical and Aerospace Engineering, University of Strathclyde, Glasgow G1 1XJ, UK*

Abstract

In this work we discuss the implementation and the performance of an in-house viscoelastic two-phase solver, is based on a diffuse interface approach. The Phase Field method is considered and the Cahn-Hilliard equation is employed for describing the transport of a binary fluid system. The interface between the two fluids adopts a continuum approach, which is responsible for smoothing the inherent discontinuities of sharp interface models, facilitating studies that are related to morphological changes of the interface, such as droplet breakup and coalescence. The two-phase solver manages to predict the expected dynamics for all the cases investigated, and presents an overall good performance. The numerical implementation is able to predict the expected physical response of the oscillating drop case, while the performance is also validated by examining the droplet deformation case. The corresponding history of the deformation is predicted for several systems considering Newtonian fluids, viscoelastic fluids and combination of both. Finally, we demonstrate the ability of the solver to capture the complex interfacial patterns of the Rayleigh-Taylor instability for different Atwood numbers when Newtonian fluids are considered. In the two regimes identified, the system is modified to consider viscoelastic fluids and the influence of elasticity is investigated.

Keywords: Two-phase flow, Phase Field method, Cahn-Hilliard, Viscoelastic fluids, Rayleigh-Taylor instability

1. Introduction

In order to investigate and analyse the complex dynamics of a multiphase system, various numerical techniques have been proposed. They are distinguished in two major categories, the *interface tracking* methods and the *interface capturing* methods [1, 2]. Tracking methods such as front-tracking [3], immersed boundary [4, 5] and boundary integral methods [6], consider a moving boundary which tracks and defines a sharp interface between the different fluids. The interface is treated explicitly and is usually described by a moving computational boundary with the interfacial conditions used as boundary conditions. These methods are very accurate since they focus on modeling the surface movement directly, however, they usually require a large amount of computational resources for storing and processing the appropriate information. Furthermore, because of mesh movement-reconstruction these methods may present singularity issues and often fail to capture morphological changes such as droplet breakup and coalescence [7–9].

The interface capturing techniques employ a static numerical mesh (fixed-grid methods) and the interface is captured based on the variation of an artificial scalar field, which is used for distinguishing between the different phases. These methods, instead of analysing the flow of two different fluid systems that are separated by an interface, consider the system as a single fluid with variable properties. With the single-fluid approach, the discontinuity across the fluid-fluid interface is eliminated and the interfacial tension is included in the equations of motion as a body force. The Volume of Fluid (VOF) [10, 11], the Level-Set (LS) [12, 13] and the Phase Field (PF) [14, 15] are all examples of interface capturing methods. The scalar quantity used as a phase indicator in all these methods is here represented by the generic variable C, which is commonly allowed to vary in the range $0 \leq C \leq 1$ (or sometimes $-1 \leq C \leq 1$) at the interface between the two fluids. In the bulk phases away from the interface the phase indicator remains constant, with $C = 0$ denoting the bulk of one of the fluids and $C = 1$ indicating the bulk of the other. For VOF and PF, this scalar quantity is usually related to a volume fraction or a mass concentration, whereas for LS it is a purely geometrical variable, defined as the signed distance function from the interface contour.

In this paper, the Phase Field method is considered for simulating two-phase flows and is implemented on top of an existing single phase computational fluid dynamics (CFD) solver originally described in Oliveira *et al.* [16]. The birth of PF theory goes back to 1893, when the first model and the basic ideas were introduced by van der Walls [17]. In his studies, van der Waals presented a new approach for the investigation of liquid-liquid interfaces, arguing that the molecules which compose both phases are in rapid movement both in the bulk of each fluid and their boundary layer. Thus, in contrast to the prevailing theory of Gibbs [18] at the time, in which the interface between two fluids is considered as a "property-barrier" (sharp interface approach), resulting in a discontinuity between

---

*Corresponding author
Email address: `k.zografos@liv.ac.uk` (Konstantinos Zografos)

the different fluid properties, van der Waals suggested that alternatively the interface should be treated as a transition region where the properties are allowed to vary continuously, resulting in a *diffuse-interface* approach. The profile of this transition region was determined by the minimisation of the free energy of the interface. Cahn and Hilliard [19, 20] extended the diffuse-interface approach and proposed a time-dependent evolution equation for investigating problems with pure diffusion. Later, Hohenberg and Halperin [21] introduced the convective Cahn-Hilliard (CH) equation known as "Model H" for binary liquids with equal densities.

In contrast with other approaches for simulating multiphase systems, diffuse-interface models become attractive for three main reasons. As discussed in Jacqmin [7] and in Yue *et al.* [8], the continuum approach of the considered interface smooths the inherent discontinuities of sharp interface models, facilitating studies that are related to morphological changes of the interface, such as droplet breakup and coalescence. In addition, they consist of a "friendlier" numerical environment able to handle and simulate demanding cases that are related to non-Newtonian fluids, in which the use of rheological models increases the challenges from a numerical point of view. Finally, their greater advantage is arguably the fact that interface tracking can be completely avoided where explicit evaluation of the interface curvature and of the interface normals is not required [22]. On the other hand the main disadvantage of PF methods, as discussed in Jacqmin [7], is the fact that they tend to produce relatively wide interfaces. Today, with the increased access to computer resources and well documented rules for approaching the sharp interface limit [7], its inherent drawback is reduced and several applications can benefit from its use [15].

Various Phase Field models have been proposed for studying interfacial phenomena and morphological changes [7, 23–25]. Anderson and Wheeler [14] reviewed the applications of the diffuse-interface models and examined the physical phenomena to which they can be applied successfully. Later, Kim [15] reviewed recent developments of the phase field models for two-phase flows and also discussed the cases of multi-component flows and their coupling with the Navier-Stokes equations. Commonly, studies of two-phase flows considering PF are done in the framework of Lattice Boltzmann (LB) methods [26], with only limited use so far with other conventional CFD techniques (i.e. Finite Volumes, Finite Elements) and these are mostly related to two-phase flows of Newtonian fluids [7, 9, 15, 27, 28]. The use of PF in the context of viscoelastic fluids flows has so far been limited, however its potential and advantages have been shown in some numerical studies in the literature, such as is in the study by Yue *et al.* [8] and the more recent by Borzacchiello *et al.* [29], Hemingway *et al.* [30] and Hemingway and Fielding [31]. Here, we discuss the implementation of the PF method in an in-house finite volume code for use with Newtonian and complex viscoelastic fluids.

The remainder of the paper is arranged as follows: In Section 2 the theory of the Phase Field method leading to the convective Cahn-Hilliard differential equation which models the second phase is presented. Also, the influence of the model parameters is discussed briefly. In Section 3, the numerical implementation of the Cahn-Hilliard equation and the treatment of each term individually is introduced. Section 4 presents the numerical results of all the various test-cases considered, appropriate for two-phase flows code validations, and the efficiency of the numerical implementation is investigated. Finally, the main conclusions of this study are summarised in Section 5.

2. Governing equations

2.1. Phase field approach

Phase Field models are based on the free energy of the fluid, first introduced and modeled by van der Waals [17]. For an isothermal and immiscible two-phase system, the free energy density f can be expressed by [17]:

$$f = \epsilon^{-1}\sigma\alpha\psi(C) + \frac{1}{2}\epsilon\sigma\alpha|\nabla C|^2, \qquad (1)$$

where C is allowed to vary in the range $0 < C < 1$ and represents the mass concentration of the system, ϵ, is the surface thickness, σ, is the interfacial tension coefficient and α, is a constant parameter that will be defined below and depends on the chosen range of the variation of C. Finally, $\psi(C)$ is a *double well* function of the mass concentration defined as

$$\psi(C) = \frac{1}{4}C^2(1 - C)^2, \qquad (2)$$

and has two energy minima located in the vicinity of each phase, as shown in Fig. 1. The double well function is the simplest non-singular function of the mass concentration [32]. Arguably it is one of the most frequently considered expressions in PF models, for modeling immiscible fluids [7], as it reduces the numerical difficulties associated with common approaches that exhibit a singular behaviour [33, 34].

The two terms on the right hand side of Eq. (1) represent two counteracting processes. The first term, $\epsilon^{-1}\sigma\alpha\psi(C)$, corresponds to the bulk energy density influenced by the double well function and generates a "phobic" behaviour. Mainly it forces the system to remain separated in two domains with pure
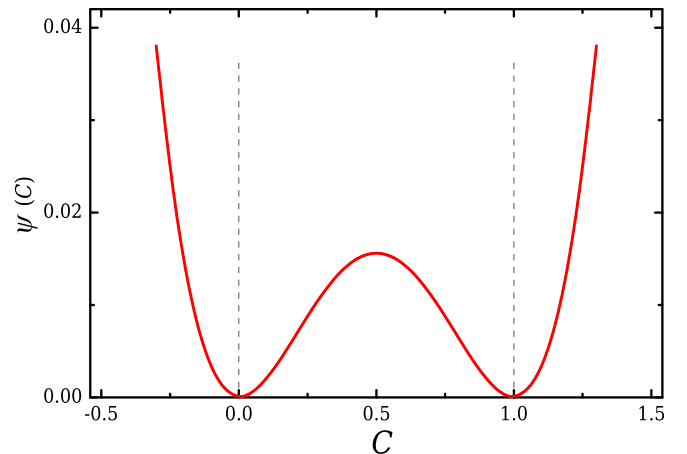

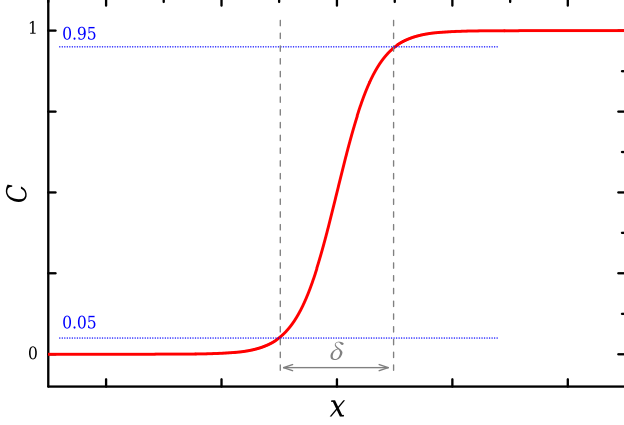Figure 1: Double well function for the free energy density model in Eq. (1).

2

Figure 2: Concentration profile at the interface of the two fluids given by Eq. (4). The *dashed* lines indicate the width of the interface and the *dotted* lines the concentration variation.

components corresponding to $C = 0$ and $C = 1$. In contrast, the energy of the system due to phase gradients, $\frac{1}{2}\epsilon\sigma\alpha|\nabla C|^2$, represents the interactions between the two components, restraining the "phobic" behaviour and enhancing a "philic" response. In other words, the first term enhances the immiscibility of the two components and the second promotes their mixing [7, 8].

The rate of change of the free energy of the system enclosed in a domain V, $F = \int_V f\, dV$, with respect to the mass concentration C, defines the chemical potential, ϕ [20]:

$$\phi = \frac{\delta F}{\delta C} = \epsilon^{-1}\sigma\alpha\psi'(C) - \epsilon\sigma\alpha\nabla^2 C, \qquad (3)$$

For a diffuse interface at equilibrium (equal counteracting effects), the chemical potential is zero and thus for a one dimensional, simple flat interface profile, Eq. (3) yields the solution profile for C [24, 27]:

$$C(x) = 0.5 + 0.5\tanh\left(\frac{x}{2\sqrt{2}\epsilon}\right). \qquad (4)$$

In this way, the concentration is allowed to vary smoothly across the interface as is shown in Fig. 2. Considering the profile of Eq. (4) a concentration variation from 0.05 to 0.95 results in a width $\delta = 4\sqrt{2}\epsilon\tanh^{-1}(0.9)$ [7, 15, 24]. As such, the parameter α of Eq. (3) should be defined as $\alpha = 6\sqrt{2}$ [15, 27]. For all numerical simulations with the PF method, δ is related to the desired number of cells, k, used for discretising the interface thickness. For a numerical (uniform) grid with characteristic cell size h, the interface width is defined as $\delta = hk$ and thus, the interface thickness is correlated to the numerical mesh as $\epsilon = hk/(4\sqrt{2}\tanh^{-1}(0.9))$ [15, 32, 35]. Furthermore, the interface thickness is usually related to the problem of interest by the Cahn number, defined as $Cn = \epsilon/L$, where L is the characteristic length of the problem and provides a measure for approaching the sharp-interface limit ($Cn \to 0$) [15, 36, 37]. In this study, the interface thickness is always analysed by five numerical cells for all considered cases ($k = 5$). More information regarding the behaviour of the method and the current implementation when k is varied can be found in Zografos

[38]. The Phase Field method was found to be sensitive to this choice [15, 39]. As explained in Kim [15], very small values of k introduce difficulties in accurately calculating the required derivatives, while for very large values of k the interface profile becomes very diffused.

2.2. Equations of motion

The convective Cahn-Hilliard equation proposed by Antanovski [23] and later employed by Gutrin *et al.* [40] was considered as an extension of the diffusion equation proposed by Cahn and Hilliard [19, 20], in order to model convection problems for incompressible, immiscible flows, taking into account the convection of the concentration C:

$$\frac{\partial C}{\partial t} + \boldsymbol{u} \cdot \nabla C = \nabla \cdot (M\nabla\phi). \qquad (5)$$

In Eq. (5), M is the mobility, a parameter that controls the magnitude of the diffusion term and naturally takes place at the molecular level (the magnitude of mobility is estimated to vary in the range $10^{-17} \lesssim M \lesssim 10^{-13}$ m^{5}s^{-1}J^{-1}, from liquid to gas phases respectively [41, 42]), $\boldsymbol{u}$ is the velocity vector and ϕ is the chemical potential introduced in Eq. (3). The convective Cahn-Hilliard equation models the creation, evolution and dissolution of phase field interfaces, which are controlled by diffusion [7, 43] and is implemented here given its ability to deal with systems composed by more than one phase. Additionally, for solving the partial differential equation, Eq. (5), the boundary conditions considered are zero-gradient at the walls of the domain for both the concentration and the chemical potential [7, 15, 24, 27]:

$$\boldsymbol{n} \cdot \nabla C = 0, \qquad (6)$$

$$\boldsymbol{n} \cdot M\nabla\phi = 0, \qquad (7)$$

where $\boldsymbol{n}$ is the unit vector normal to the domain boundary. The no-flux boundary condition imposed by the Newman boundary condition for the chemical potential (Eq. (7)) arises directly from the conservation of mass, as is detailed and discussed in the studies of Ding *et al.* [27] and Kim [15].

Considering a two-phase (binary) fluid system the continuity and the incompressible Navier-Stokes equation are:

$$\nabla \cdot \boldsymbol{u} = 0, \qquad (8)$$

$$\rho\left(\frac{\partial \boldsymbol{u}}{\partial t} + \boldsymbol{u} \cdot \nabla \boldsymbol{u}\right) = -\nabla p + \nabla \cdot \boldsymbol{\tau} + \rho\boldsymbol{g} + \boldsymbol{f}_{\text{st}}, \qquad (9)$$

where ρ is the density, p the pressure, $\boldsymbol{\tau}$ the extra stress tensor, $\boldsymbol{g}$ the gravitational acceleration vector and the last term, $\boldsymbol{f}_{\text{st}}$, is added to account for the forces due to interfacial tension.

The modeling of the surface forces in the Navier-Stokes equation is key to a successful numerical code, and various models have been proposed for that reason [7, 8, 22, 25, 32]. Here, the work of Badalassi *et al.* [24] and Ding *et al.* [27] is adopted and the applied forces are evaluated based on the gradients of the concentration across the interface:

$$\boldsymbol{f}_{\text{st}} = \phi\nabla C. \qquad (10)$$

3

The advantage of this approach is that it is easier to implement since there is no need to evaluate gradient normals and additionally it has shown very good performance compared to the LS method as discussed in Amiri and Hamouda [28].

Here, the cases considering viscoelastic fluids employ the Oldroyd-B and the Upper Convected Maxwell (UCM) [44] models, be expressed by

$$\lambda \overset{\triangledown}{\boldsymbol{\tau}}_p + \boldsymbol{\tau}_p = \eta_p(\nabla \mathbf{u} + \nabla \mathbf{u}^T), \qquad (11)$$

where $\overset{\triangledown}{\boldsymbol{\tau}}_p$, is the upper-convected derivative of the polymeric component of the extra-stress tensor, $\boldsymbol{\tau}_p$ and η_p the polymeric viscosity and λ the relaxation time of the polymer. The stress-tensor in Eq. (9) is decomposed as $\boldsymbol{\tau} = \boldsymbol{\tau}_p + \boldsymbol{\tau}_s$, where $\boldsymbol{\tau}_s = \eta_s(\nabla \boldsymbol{u} + \nabla \boldsymbol{u}^T)$ and corresponds to the solvent contributions to the stresses. The ratio of the solvent viscosity, η_s, to the total zero shear viscosity, $\eta = \eta_s + \eta_p$, known as solvent viscosity ratio, β, needs to be defined and gives an indication of the contributions of each part to the total stress tensor. For the UCM, $\eta_s = 0$ and the extra tensor is solely the polymeric part.

Concluding, the physical properties of a binary fluid (ρ, η, η_s, η_p and λ) that is composed of the phases labeled as 1 and 2, should remain constant in the bulk of each phase and vary across the interface. Here, all physical properties are considered as a linear function of the concentration and are expressed by

$$\theta(C) = \theta_1 C + \theta_2(1 - C), \qquad (12)$$

where θ indicates a generic physical property. Additionally, for all investigated cases the ratio between the properties of the fluids considered is reported and is defined in generic form as $\lambda_\theta = \theta_1/\theta_2$.

3. Numerical implementation

In this section the discretisation of the Cahn-Hilliard equation and of the surface forces in the momentum equation are presented. The equations including the second phase are implemented on top of the in-house viscoelastic single-phase solver. The key ideas and principles of the single phase solve are discussed extensively in [16, 45, 46] and will not be repeated here. In this study, we solve directly for the polymeric part of the stresses (Eq. (11)) following the standard approach as described in detail in [16]. In the following discussion we adopt the same notation with those studies and the discretisation is in a similar fashion to the standard Finite Volume method for collocated grids described in Ferziger and Perić [47] amongst others. A more detailed description of the intermediate steps followed can be found in Zografos [38].

3.1. Cahn-Hilliard discretisation

The combination of Eq. (3) and Eq. (5) will result in a fourth order concentration gradient, which makes the discretisation of Eq. (5) very complex. In order to overcome this difficulty, we slightly modify the known form of CH equation given in Eq. (5), by introducing a diffusive flow rate $\boldsymbol{q} = M\nabla \phi$, to read

$$\frac{\partial C}{\partial t} + \boldsymbol{u} \cdot \nabla C = \nabla \cdot \boldsymbol{q}. \qquad (13)$$
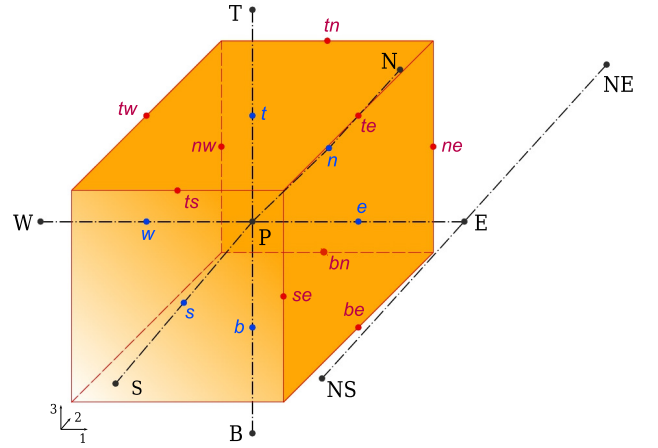

Figure 3: Three dimensional representation of a control volume. Cell centres are indicated by *black-dots*, cell faces by *blue-dots* and edge centres by *red-dots*.

By doing this the chemical potential is explicitly evaluated at each computational cell of the discretised domain using Eq. (3) and the current-time concentration values. The Laplacian term of the concentration in Eq. (3) is discretised considering a second order approximation as

$$\left(\nabla^2 C\right)_{\mathrm{P}} = \left(\frac{\partial^2 C}{\partial x_i^2}\right)_{\mathrm{P}} = \frac{C_{\mathrm{E}} + C_{\mathrm{W}} + C_{\mathrm{N}} + C_{\mathrm{S}} + C_{\mathrm{T}} + C_{\mathrm{B}} - 6C_{\mathrm{P}}}{\Delta h^2},$$
$$(14)$$

using the stored values on each cell centre similar with the approach of Kim [15]. The abbreviations E, W, N, S, T and B correspond to the six neighbouring cell-centres of the 3D computational cell P and are shown schematically in Fig. 3. Then, together with the mobility, they are used for the evaluation of a general diffusive flow rate of Eq. (13).

In the studies of Kim [25] and Ding *et al.* [27], the mobility is defined as a second order function of the concentration:

$$M = M_c C(1 - C). \qquad (15)$$

In this study, we follow the same approach and its behaviour is shown schematically in Fig. 4. We note, that the mobility can also be treated as constant, $M = M_c$ [8, 48]. Although in the literature the choice of a constant or a variable mobility is not clearly justified, based on the physical meaning of mobility (see discussion in Section 2.2) it seems a more natural choice to employ a function like the one shown in Fig. 4, rather than a constant. In this way, M is explicitly zero at the bulk of each phase, implying that there is no diffusion of concentration (and thus of the fluid properties) in the bulk of the same phase. A short discussion on the effects of the choice of the characteristic mobility following this approach can be found in Zografos [38]. It was found that variations in the values of characteristic mobility do not produce significant differences in the evaluation of the pressure drop along the interface.

The discretisation of all equations is done considering a generalised coordinate system (ξ_l, $l = 1, 2, 3$) [16]. Equation (13)
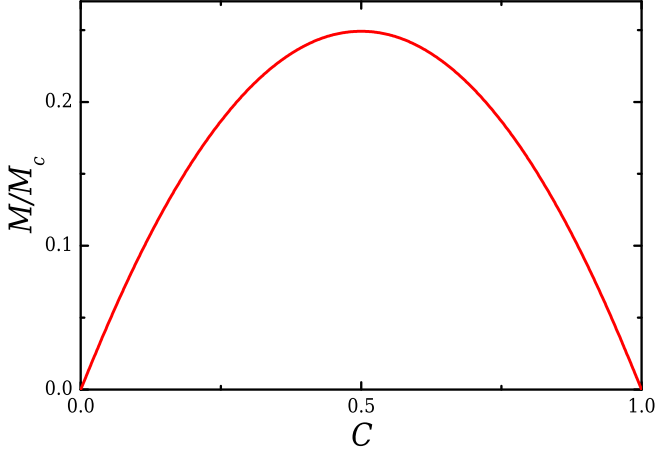
4

Figure 4: Normalised profile for the mobility along the interface using Eq. (15).

can be expressed using Einstein notation in a Cartesian coordinate system $(x_i, i = 1, 2, 3)$ as

$$\frac{\partial C}{\partial t} + u_i \frac{\partial C}{\partial x_i} = \frac{\partial q_i}{\partial x_i}. \tag{16}$$

Employing the coordinate transformation rules for expressing the time and spatial derivatives in a generalised coordinate system [47], each term of Eq. (16) is transformed as follows:

• Inertia term

$$\frac{\partial C}{\partial t} = \frac{1}{J} \frac{\partial}{\partial t} (CJ). \tag{17}$$

• Convective term

$$\frac{\partial}{\partial x_i} (u_i C) = \frac{1}{J} \frac{\partial}{\partial \xi_l} \left(C u_i \beta^{li} \right). \tag{18}$$

• Diffusive term

$$\frac{\partial q_i}{\partial x_i} = \frac{1}{J} \frac{\partial}{\partial \xi^l} \left(q_i \beta^{li} \right), \tag{19}$$

where J is the Jacobian of the transformation and β^{ij} are the co-factors of the coordinate transformation matrix. Hence, Eq. (16) is expressed in a generalised coordinate system as

$$\frac{\partial}{\partial t} (CJ) + \frac{\partial}{\partial \xi_l} \left(C u_i \beta^{li} \right) = \frac{\partial}{\partial \xi^l} \left(q_i \beta^{lj} \right), \tag{20}$$

where the components of the diffusive flow rate of Eq. (13) are expressed in the generalised coordinate system as

$$q_i = \frac{M}{J} \frac{\partial \phi}{\partial \xi^l} \beta^{li}, \tag{21}$$

Since the finite-volume approach is adopted here, Eq. (20) is integrated over a numerical cell of volume V_P and the CH equation is expressed in an integral form as

$$\int_{V_P} \frac{\partial}{\partial t} (CJ) \, dV_P + \int_{V_P} \frac{\partial}{\partial \xi_l} \left(C u_i \beta^{li} - q_i \beta^{li} \right) dV_P = 0. \tag{22}$$

More details can be found in Zografos [38]. Employing the divergence theorem the discretised form of the integrated Cahn-Hilliard equation is obtained, with each term examined separately below:

• Inertia term

Integrating Eq. (17) over a 3D computational cell will give:

$$\int_{V_P} \frac{\partial}{\partial t} (CJ) \, dV_P = \left(\frac{C^n - C^{n-1}}{\Delta t} \right)_P V_P \tag{23}$$

where C^n and C^{n-1} are the cell-centred solutions of the concentration at the current and previous time step, respectively. For all the following discretisations, both the convective and the diffusive terms are evaluated using concentration values computed at the current time, following the fully-implicit considerations of the single-phase solver of Oliveira et al. [16]. For that reason, the index n is dropped to avoid confusion and only the previous time step level will be indicated if needed.

• Convective term

As previously, integrating now Eq. (18) over a 3D computational cell will yield:

$$\int_{V_P} \frac{\partial}{\partial \xi_l} \left(C u_i \beta^{li} \right) dV_P = \left(C u_i \beta^{1i} A \right)_w^e + \left(C u_i \beta^{2i} A \right)_s^n + \left(C u_i \beta^{3i} A \right)_b^t$$
$$= \sum_{f=1}^{6} \left(\sum_i \hat{C}_f u_i b_f^{li} \right), \tag{24}$$

where the convected variable $\hat{C}_f$ indicates that a high resolution approach is employed for evaluating the convective variable at the cell face f, along the appropriate direction of each of the six-faces (e, w, n, s, t and b, shown schematically in Fig. 3) of the computational cell P, following the same procedure as discussed in Oliveira et al. [16] and in Alves et al. [46]. The variables b_f^{li} appearing in the last expression are evaluated from the product $b_f^{li} = \beta^{li} A_f$ where the subscript f indicates the appropriate face of the CV, as explained in Perić [49].

• Diffusive term

The integrated diffusion term of the generalised Cahn-Hilliard Eq. (19) is:

$$\int_{V_P} \frac{\partial}{\partial \xi^l} (q_i \beta^{li}) dV_P = \left[(q_1 \beta^{11} + q_2 \beta^{12} + q_3 \beta^{13}) A \right]_w^e$$
$$+ \left[(q_1 \beta^{21} + q_2 \beta^{22} + q_3 \beta^{23}) A \right]_s^n$$
$$+ \left[(q_1 \beta^{31} + q_2 \beta^{32} + q_3 \beta^{33}) A \right]_b^t = \sum_{f=1}^{6} b_f^{li} q_i = S_{C,dif} \tag{25}$$

Arranging all the discretised terms together, the linear algebraic system that is solved numerically is:

$$a_P C_P - \sum_F a_F C_F = S_{C,dif} + \frac{V_P}{\Delta t} C_P^{n-1}. \tag{26}$$

3.2. Surface forces discretisation

In continuum surface modeling, the surface forces are usually evaluated by a product of an interface gradient and the surface curvature [50]. For all approaches of this kind, the effects of the surface force are taken into account by considering

5

a form of a volume force, f_{st}, which is added in the momentum equation (cf. Eq. (9)). For the PF method, various different approaches have been proposed for evaluating the effects of the surface forces [7, 22, 25, 27]. Here, the product of the chemical potential, ϕ, and the gradient of the concentration, C, as in Ding *et al.* [27] is used (see Eq. (10)).

Following the same concepts as in Section 3.1, the interfacial tension force in generalised coordinates is expressed as

$$f_{st} = \phi \frac{\partial C}{\partial x_i} = \phi \frac{1}{J} \frac{\partial C}{\partial \xi_l} \beta^{li}. \tag{27}$$

The force term component acting along each one of the three directions is added as a source term in the appropriate component of the momentum equation, following the same approach as described in Oliveira *et al.* [16] for the pressure gradient terms. The Jacobian in Eq. (27) cancels out when the momentum equation is expressed in generalised coordinates [16] and is only considered with the gravity terms. The values of the chemical potential are known and therefore for all three directions the evaluation of the surface forces is done on the cell centres P. The discretised expression of the surface forces is

$$\int_{V_P} \phi \frac{\partial C}{\partial \xi_l} \beta^{li} dV_P = \sum_{l=1}^{3} \phi_P b^{li} [\Delta C]_l^P = S_{u_i-st}, \tag{28}$$

and as mentioned is added in the sources of the momentum equation. The total sources in the momentum equation considering also those reported in Oliveira *et al.* [16] can be summarised as

$$S_{u_i} = S_{u_i-pressure} + S_{u_i-stress} + S_{u_i-gravity} + S_{u_i-st} + S_{u_i-diffusion}. \tag{29}$$

The solution procedure is as follows. Starting from an initial guess of the two phases, the stress field is evaluated and then the velocity field is corrected based on the SIMPLEC algorithm procedure [16]. Then, the transport equation of the concentration is solved by the discretised Cahn-Hilliard. Similarly to the momentum algebraic equations, the matrices of the linear algebraic system (cf. Eq. (26)) are pre-conditioned by an incomplete LU decomposition and solved with the bi-conjugate gradient method [16].

3.3. The boundary conditions

The numerical implementation of the Cahn-Hilliard equation is concluded with the boundary conditions. As mentioned in Section 2, the appropriate boundary conditions for CH result in zero gradients on the normal direction of the boundary for both the concentration and the chemical potential (see Eqs. (6) and (7)). Therefore, it suffices to declare explicitly that the face centre has the same value as the boundary cell centre:

$$\begin{aligned} C_f &= C_{P,bnd}, \\ \phi_f &= \phi_{P,bnd}, \end{aligned} \tag{30}$$

where f indicates the boundary face centre (e, w, n, s, t or b) along the appropriate direction. The evaluation of the concentration gradients at the boundaries that results from the surface force as discussed in Section 3.2, are explicitly taken as being equal to zero [38], thus obeying directly Eq. (30).

4. Results and discussion

The implementation of the Cahn-Hilliard equation on top of the single-phase viscoelastic solver is validated here and the performance of the two-phase solver is assessed. Two sets of test cases are considered: (i) active interfacial tension ($\sigma \neq 0$) cases and (ii) non-active interfacial tension ($\sigma = 0$) cases. The performance of the solver is validated under various conditions while for the latter case, two-phase instabilities when viscoelastic fluids are considered are also examined.

4.1. Active interfacial tension ($\sigma \neq 0$)

In this section, the interfacial tension forces are taken into account and the numerical implementation and its ability to predict the expected behaviour for two different test cases is examined: the case in which the evolution of an initially square Newtonian droplet surrounded by a Newtonian fluid towards its equilibrium shape is monitored; the case in which the deformation of a droplet submitted to constant shear is studied for combinations of Newtonian and viscoelastic fluids.

4.1.1. Oscillating droplet

A Newtonian square 2D drop (ρ_2, η_2) is initially set in the middle of a square domain of width H and is surrounded by a Newtonian matrix fluid (ρ_1, η_1), as shown in the first contour-plot (top left) of Fig. 5. The drop is initialised to have sides of size $d = H/2$, while the density and viscosity ratios are $\lambda_\rho = \rho_1/\rho_2 = 100$ and $\lambda_\eta = \eta_1/\eta_2 = 100$. Gravitational forces are not taken into account in this test and thus, viscous forces are the most important. In order to report our results, we define a dimensionless time as $\tilde{t} = t/t_{vis}$ where, t is the current time under examination and t_{vis} is the characteristic viscous time [51], defined here as $t_{vis} = \Delta_\eta R_{eff}/\sigma$. The effective radius is approximated as $R_{eff} = 2d/\sqrt{\pi}$, while $\Delta_\eta = \eta_1 - \eta_2$. The Cahn number for this case is $Cn = \epsilon/R_{eff} = 0.017$ and $\epsilon/h = 0.60$. The concentration is initialised as $C = 0$ inside the drop, $C = 1$ in the matrix fluid and is allowed to vary along the interface as described in Section 2.1 using Eq. (4).

The aim of this typical numerical test for two-phase flows is to verify whether the numerical implementation is able to capture the expected behaviour of the drop, which is to move from the initial unstable state towards equilibrium. The initial drop shape is highly unstable since the four corners are characterised by strong concentration gradients, in accordance with the existence of locally higher levels of curvature. Since the interfacial tension is proportional to the interface curvature, the initial square-shaped drop is expected to deform due to an interfacial tension imbalance along the interface. This in turn triggers a pressure imbalance in the momentum equation, which results in a velocity field that has an oscillatory behaviour and moves the interface. This exact behaviour is well captured in our numerical simulations as it can be seen in Fig. 5 (and in the video in Supplementary Material). At early times the drop is changing shape in time. The oscillatory movement caused by the velocity field gradually decays and the drop eventually reaches an equilibrium state and comes to a rest, where the stable equilibrium circular shape is attained [50, 52]. Here, only

a quarter of the geometry is considered, corresponding to the top left quarter, indicated in the first contour at $\tilde{t} = 0$ of Fig. 5. In Appendix A a short discussion regarding the dependency of the obtained numerical solutions upon the employed numerical meshes is given, illustrating that our results are not sensitive to mesh refinement.

Figure 6 illustrates the magnitude of the generated normalised velocity field (left half-part) and the normalised pressure
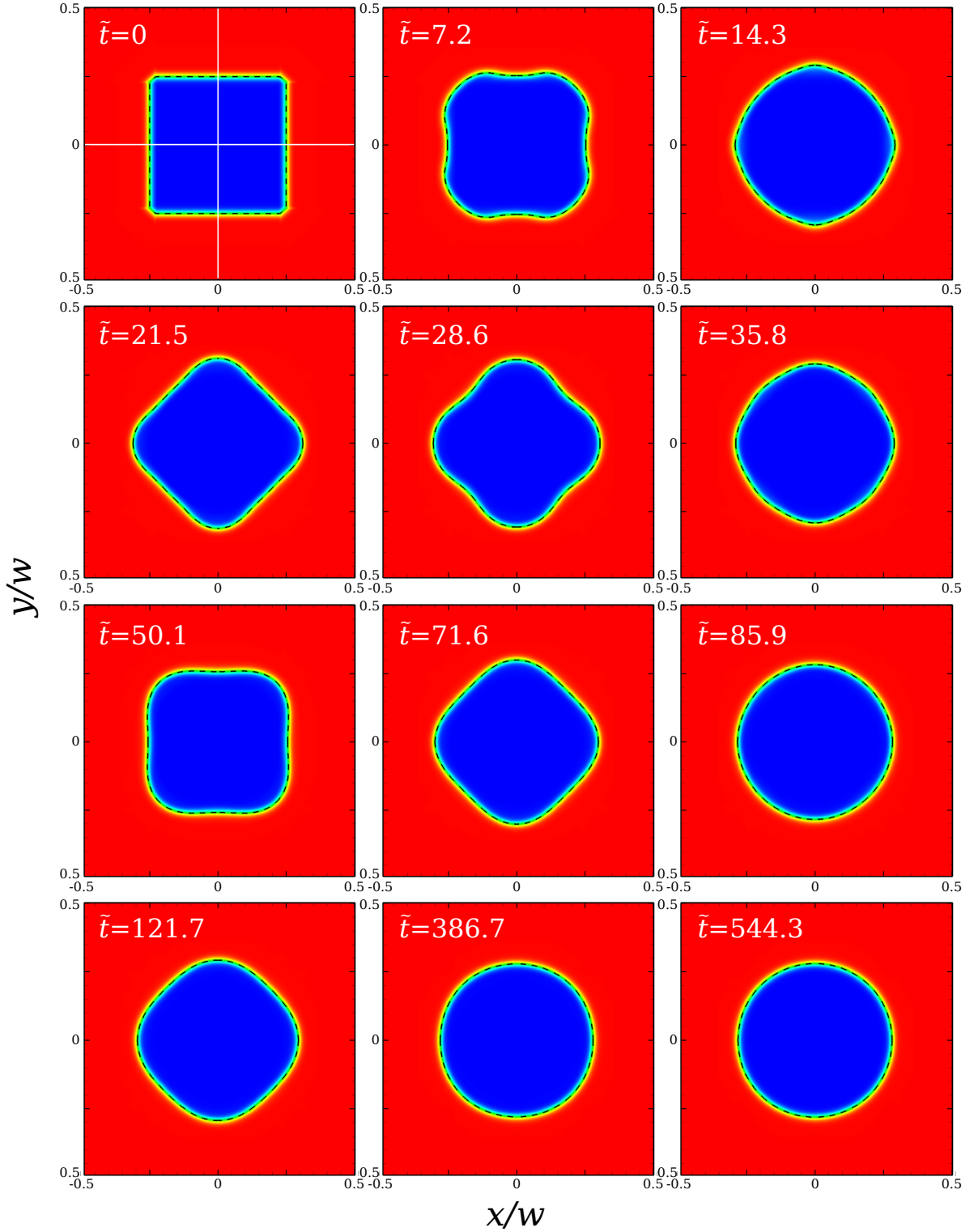

Figure 5: Contour-plots of the concentration of the Newtonian two-phase system with $\lambda_\rho = \lambda_\eta = 100$, illustrating the droplet shape at different dimensionless times. The *dashed* line indicates the 0.5-contour where the interface position is considered.

7
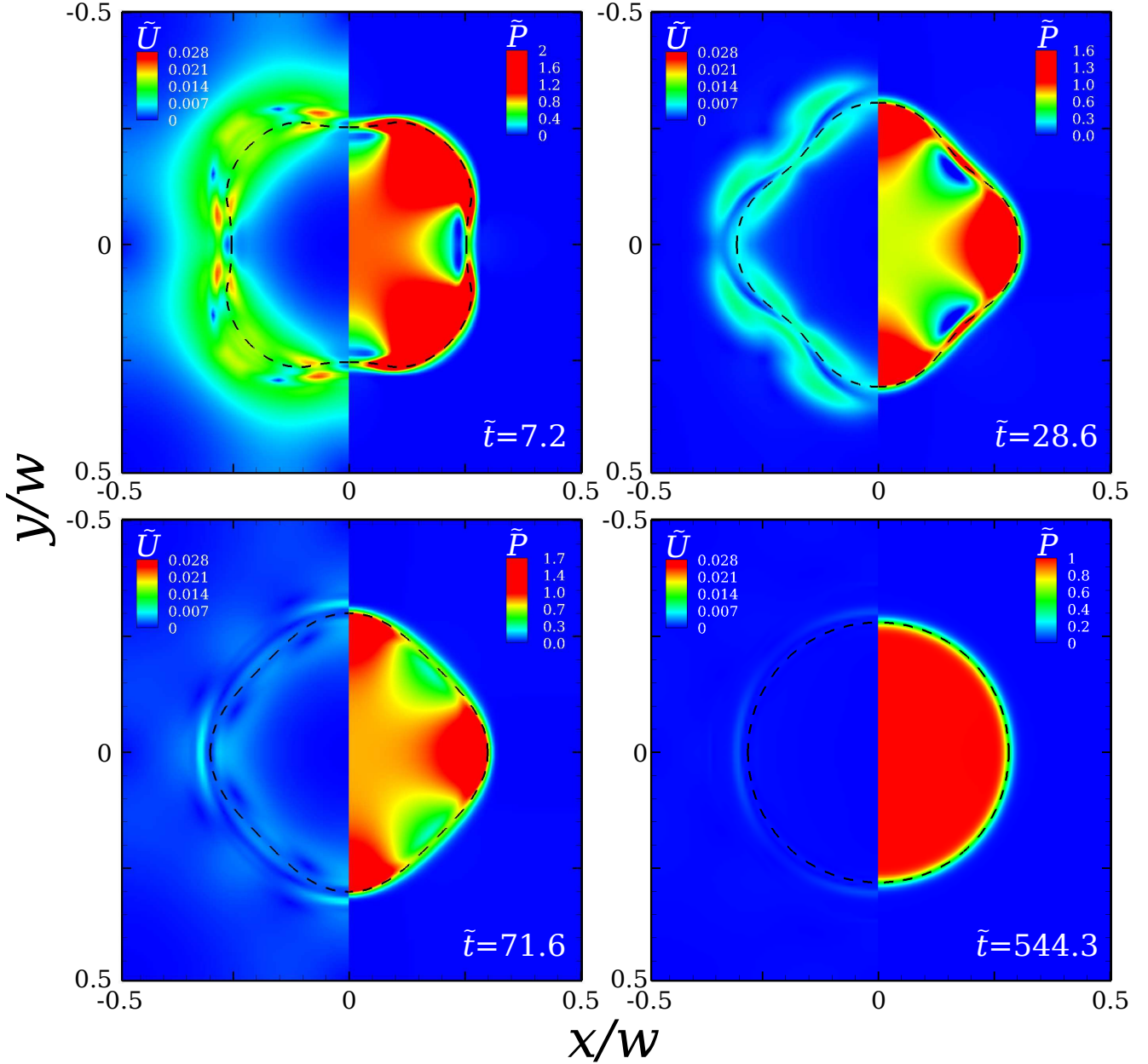
Figure 6: Combined contour-plots of the velocity magnitude (left-part) and the pressure distribution (right-part) at different dimensionless times for $\lambda_\rho = \lambda_\eta = 100$. The *dashed* line indicates the 0.5-contour where the interface position is considered.

field (right half-part) around the droplet for four different time-frames. For each one of them, a new position with different locations of higher curvature is generated, resulting in the equivalent regions where the pressure has higher values. The contour-plots related to pressure distribution are coloured based on the normalised pressure values at equilibrium, $\tilde{P} = P/P_{char}$, where P_{char} is the expected capillary pressure at equilibrium defined as $P_{char} = \sigma/R_{eff}$ (i.e. 2D Young-Laplace formula). For the time-frames $\tilde{t} = 7.2$, $\tilde{t} = 28.6$ and $\tilde{t} = 71.6$, the pressure varies along the interface and generates the velocity field that is shown in the left-half in normalised values of the velocity magnitude $\tilde{U}$. The normalisation of the velocity field is achieved by considering a characteristic capillary velocity $U_{char} = \sigma/\Delta_\eta$ [51]. As the

experiment evolves in time, the velocity field exhibits smaller values and the oscillation gradually decays, yielding a circular droplet at $\tilde{t} = 544.3$. At equilibrium, the pressure field varies only across the interface, corroborating the expected behaviour. In the numerical results, the final radius of the droplet deviates 0.4% from R_{eff}, while the resulted pressure drop along the interface deviates approximately 1% from the expected value of the Young-Laplace formula.

An extensive evaluation of the capability of our implementation to evaluate the expected pressure drop by the Young-Laplace formula along the interface has been performed in Zografos [38]. The performance of the implementation was accomplished for a range of different radii, interfacial tension co-
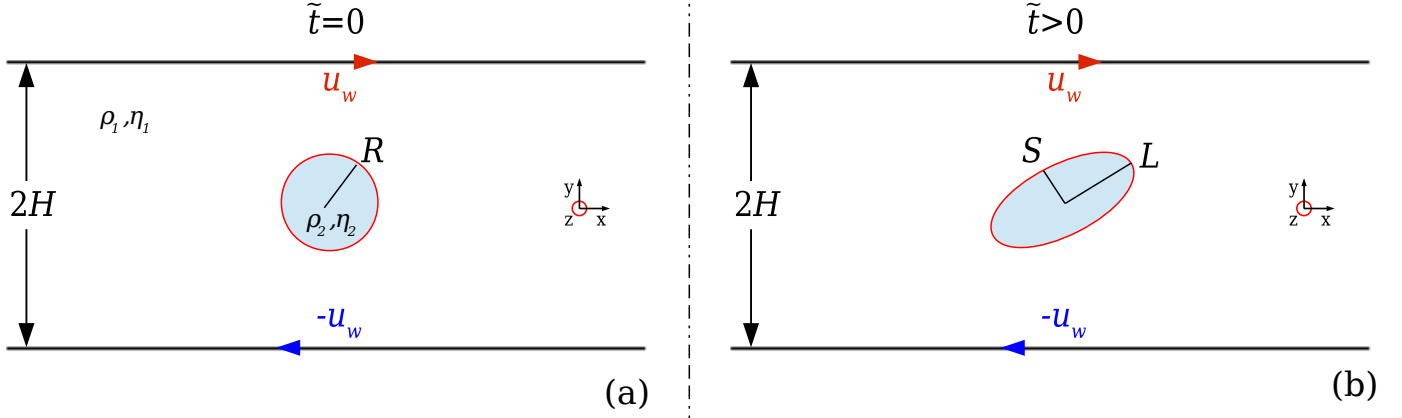
Figure 7: Configuration for the shear deformation test-case. The drop is positioned in between the two parallel plates ($y = 0$) that move in opposite directions with the same velocity (a), and deforms under constant shear obtaining an ellipsoidal form (b).

efficients and different viscosity and density ratios, indicating the correct implementation and efficiency of PF method.

4.1.2. Droplet deformation under constant shear

The study of a droplet deformation under shear [53] is one of the most commonly-considered test cases for validating two-phase flow implementations [54, 55]. For this test-case, the drop is placed between two parallel plates that move with constant velocities in opposite directions, as shown in Fig. 7a. The generated velocity field deforms the drop, with the deformation depending on the viscosity ratio, λ_η, and the capillary number, Ca, that represents a measure of the viscous to interfacial tension effects. Taylor [53], showed that when a liquid drop is surrounded by a matrix liquid of equal viscosity ($\lambda_\eta = 1$), its deformation under a constant shear-rate takes an ellipsoidal form and can be expressed by the deformation parameter:

$$D = \frac{L - S}{L + S} \tag{31}$$

where L is the longest and S the shortest axes of the ellipsoidal deformation, as shown schematically in Fig. 7b. Here, the distance between the two plates is 2H and the centre of the drop with radius R, is equidistantly placed between the plates. In the absence of the drop, the velocity field generated by the opposite movement of the two plates is known and has an analytical solution:

$$u = \frac{u_w}{H} y, \tag{32}$$

where $\dot\gamma = u_w/H$ is the characteristic shear-rate. This velocity field is applied as an initial condition for the simulations.

We examine four different cases that describe the system drop-matrix fluid: (i) Newtonian drop inside a Newtonian matrix (NN); (ii) Newtonian drop inside a viscoelastic matrix (NV); (iii) Viscoelastic drop inside a Newtonian matrix (VN) and (iv) viscoelastic drop inside a viscoelastic matrix (VV). We compare our results with the study performed by Chinyoka *et al.* [54]. These authors investigated the same four cases and their two-phase systems was modeled using the Level-Set method.

The dimensionless numbers characterising all the cases examined are the capillary number, defined as $Ca = \eta_1 \gamma R/\sigma$ and the Reynolds number, defined as $Re = \rho_1 \gamma R^2/\eta_1$. For the cases of viscoelastic fluids, the viscoelastic phases are modeled using the Oldroyd-B model, where the Weissenberg number is defined as $Wi = \lambda\dot\gamma$. In the above definitions, η_1 and ρ_1 are the viscosity and the density of the matrix fluid respectively. For the relaxation time, λ, when we investigate combinations of Newtonian and viscoelastic fluids, there is only one relaxation time ($\lambda = 0$ for Newtonian fluids) and therefore for these cases we do not define a relaxation time ratio. For the case of VV, both fluids are considered to have the same relaxation time, $\lambda_1 = \lambda_2$, and thus $\lambda_\lambda = 1$. For all cases the drop is set with an initial radius $H/R = 4$, while the matrix fluid has the same viscosity and the same density as the drop ($\lambda_\eta, \lambda_\rho = 1$). We set $Ca = 0.6$ and $Re = 0.3$, while for the cases with viscoelastic fluids the Weissenberg number is set to $Wi = 0.4$. The boundary walls at $y = H$ and $y = -H$ are moving with equal but opposite velocities, while the right and left boundaries of the domain are treated with symmetry boundary conditions. The choice of these conditions will generate a flow field that rotates clockwise (based on the direction the walls move as shown in Fig. 7) in-

Table 1: Mesh characteristics for the study of the droplet deformation under constant shear. All meshes are uniform in the region of interest ($4H \times 2H$).

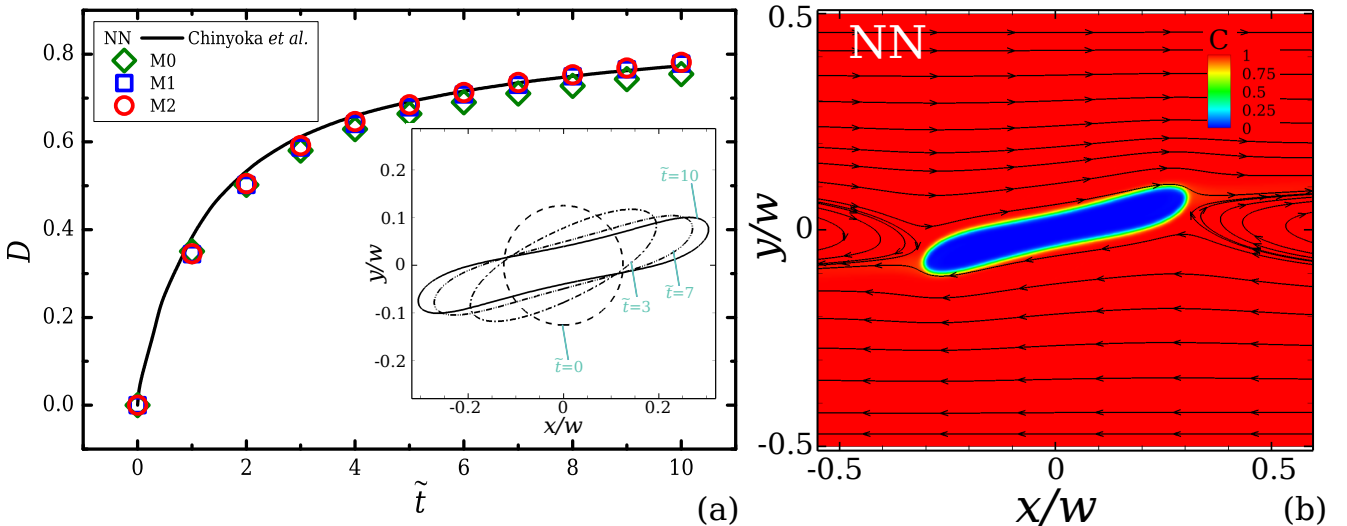| Mesh	$\delta x_{min}/2H = \delta y_{min}/2H$	$Cn = \epsilon/R$	ϵ/h	#Cells
M0	0.008	0.038	0.60	50,688
M1	0.006	0.027	0.60	90,000
M2	0.004	0.019	0.60	166,912

Figure 8: Drop deformation in dimensionless time, evaluated using Eq. (31), for all numerical grids of Table 1, compared with the solution from Chinyoka *et al.* [54]. Drop deformation indicated by the 0.5-contour for various dimensionless times (a), and contour-plot of concentration together with the streamlines at $\tilde{t} = 10$ (b), for $Ca = 0.6$ and $Re = 0.3$.

side the numerical domain and for that reason it is important to select a domain that is long enough ($40H$) to avoid any artificial disturbances to the region of interest ($4H \times 2H$), induced by the boundaries. Table 1 presents the relevant information for all meshes considered. For the NN case three meshes considered, while for the rest M1 and M2 are employed.

The first case discussed is that of a Newtonian drop inside a Newtonian matrix fluid. Figure 8 shows the history of the deformation evaluated by the 0.5-contour of C at different dimensionless times, defined as $\tilde{t} = t\dot{\gamma}$. The numerical results for all the numerical meshes considered are compared with the results reported by Chinyoka *et al.* [54]. The deforming drop follows the same behaviour reported by these authors, with the deformation increasing continuously in time. It can be seen that the results obtained for the M1 and M2 meshes are almost identical deviating approximately 1% from those of Chinyoka *et al.* [54]. The inset image of Figure 8a, illustrates the drop deformation based on the 0.5-contour at four dimensionless times $\tilde{t} = 0$, $\tilde{t} = 3$, $\tilde{t} = 7$ and $\tilde{t} = 10$. Figure 8b shows the contours of concentration at the last time of the evaluated deformation $\tilde{t} = 10$, together with the velocity streamlines around the deformed drop. Obviously, the presence of the drop changes the velocity field significantly which is no longer well described by Eq. (32): the matrix fluid flowing towards the poles of the drop is forced to change direction and flows backwards, whereas the rest is flowing around the deformed interface and constantly increases the deformation. The development of the stresses along the interface is responsible for the history and the trend of the deformation. Therefore, this deformation is expected to vary differently in time depending on the viscosity ratio λ_η, Ca and Re, which have a direct impact on the stress field. Minor deviations relative to the results of Chinyoka *et al.* [54] are observed at early times. These could be due to possible spurious velocities that influence more at these stages and depend on the method employed (e.g. PF, LS, etc.) or the approach of the sur-face forces, while the discretisation method and different numerical schemes introduce additional errors.

In order to evaluate the performance of our two-phase solver when viscoelastic fluids are employed we initially modify the NN system presented before to the case of a Newtonian drop inside a viscoelastic matrix fluids (NV). As it can be seen from Fig. 9a, our results are in agreement with Chinyoka *et al.* [54], confirming their observations that a Newtonian drop settles to a stationary state within a viscoelastic matrix fluid. The deformation obtained for the NV case at time $\tilde{t} = 10$ is shown in Fig. 9b, demonstrating the contours of the concentration and the generated streamlines. As explained in Chinyoka *et al.* [54] this behaviour is related to the presence of higher first normal-stress differences that force the Newtonian drop to align more along the flow direction, thus leading to a lower deformation angle compared to the NN case. In Fig. 9c the behaviour obtained for a viscoelastic drop within a Newtonian matrix fluid (VN) is shown, demonstrating again an agreement with the reported behaviour by Chinyoka *et al.* [54]. In contrast with the NV case the alignment of the drop along the flow direction is now lower than before, allowing shear forces at the interface to increase the drop deformation as shown in Fig. 9d for $\tilde{t} = 10$. Finally, Fig. 9e shows the reported behaviour of a viscoelastic drop within a viscoelastic matrix (VV) and Fig. 9f illustrates the corresponding shape, concentration field and streamlines for $\tilde{t} = 10$. It can be clearly seen that the drop in this case exhibits a smaller deformation than the two previous cases, similarly to what was observed by Chinyoka *et al.* [54].

Overall our results show that we are able to capture the same behaviour as exhibited in Chinyoka *et al.* [54]. In agreement with their observations, we see that by introducing elasticity either by modifying the drop (VN), the matrix fluid (NV) or both (VV), the overall deformation of the drop due to shear is reduced relative to the behaviour predicted for the NN system.
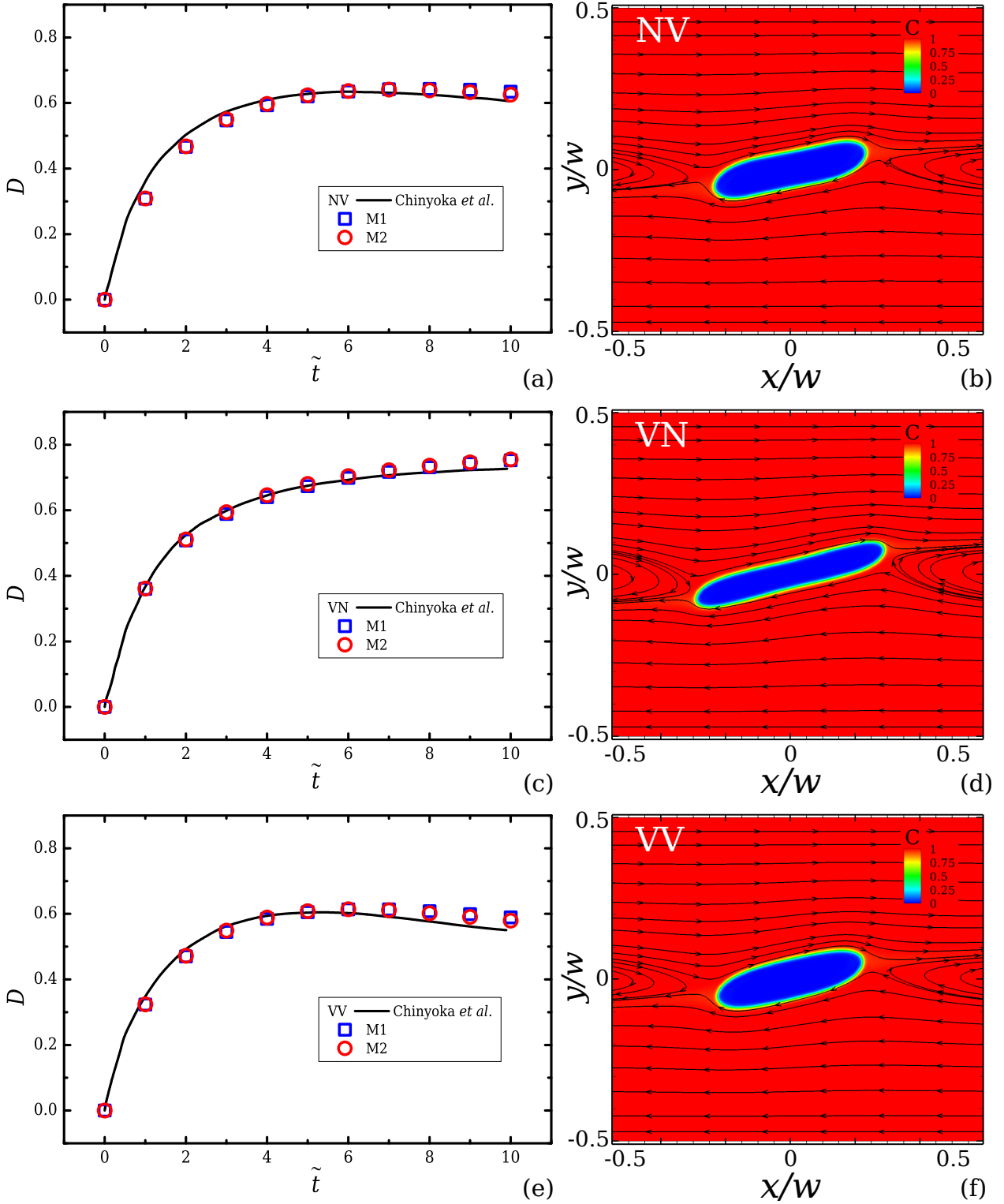
Figure 9: Drop deformation for (a) the NV case and (b) the corresponding contour-plot of concentration together with the streamlines at $\tilde{t} = 10$, for (c) the VN case and (d) the corresponding contour-plot of concentration together with the streamlines at $\tilde{t} = 10$, for (e) the VV case and (f) the corresponding contour-plot of concentration together with the streamlines. All cases are compared with the equivalent solutions reported in Chinyoka *et al.* [54].

4.2. Non-active interfacial tension ($\sigma = 0$): The 2D Rayleigh-Taylor instability

The existence of a perturbation along the interface between two fluids with a different density results in an instability known as the Rayleigh-Taylor instability [56, 57] and is investigated in this section for Newtonian and viscoelastic fluids. In this problem the driving mechanism is the gravitational forces that act when a more dense (heavy) fluid is placed on top of a less

11

dense (light) fluid. The resulting instability evolves in different ways depending on the density differences and the influence of viscous forces [58, 59]. We therefore divide this section into two subsections, based on the influence of viscosity. First, the case near the inviscid limit is investigated and then we report our results within the viscous regime. The effect of the interfacial tension coefficient is considered to be negligible for all the cases examined and is explicitly set to zero. This generates a zero chemical potential ($\phi = 0$) everywhere (cf. Eq. (3)) and the diffusion term in the Cahn-Hilliard equation is neglected, with only the convection of the concentration taken into account (see Eq. (5)).

The density difference for the Rayleigh-Taylor instability problem is commonly represented by the Atwood number [57, 58, 60], which is defined as

$$At = (\rho_1 - \rho_2)/(\rho_1 + \rho_2), \tag{33}$$

where ρ_1 and ρ_2 are the densities of the more dense and less dense fluids respectively. The influence of viscous effects are evaluated by introducing a density-weighted average viscosity [61] defined as

$$\nu = (\eta_1 + \eta_2)/(\rho_1 + \rho_2). \tag{34}$$

Here, for all the cases considered the viscosity of the two fluids is set to be the same ($\lambda_\eta = 1$). The Reynolds number that characterises the problem is defined as in Ding *et al.* [27]:

$$Re = \rho_1 w^{3/2} g^{1/2}/\eta, \tag{35}$$

where w is the width of the domain. For the cases of viscoelastic fluids presented, we always consider a heavy viscoelastic fluid on top of a light viscoelastic fluid with same relaxation times ($\lambda_\lambda = 1$), while their behaviours are evaluated by the UCM model (i.e. $\beta = 0$). The Weissenberg number of the problem which describes the relative importance of elastic to viscous forces in the flow and is defined as

$$Wi = \lambda(g/w)^{1/2}. \tag{36}$$

4.2.1. Approximately inviscid limit

This regime has been extensively investigated in two-phase flow studies considering a system of two Newtonian fluids (NN), and is now established as one of the benchmarks for examining the capability of a numerical implementation to track the evolution of the interface [7, 15, 27, 60, 62, 63]. The ability of a numerical solver to capture effectively the different patterns of the occurring instabilities indicates its potential for investigating more complex problems.

Tryggvason [60], investigated numerically this instability and reported its evolution for inviscid, incompressible, Newtonian fluids with zero interfacial tension for $At = 0.5$ and $At \simeq 1$.
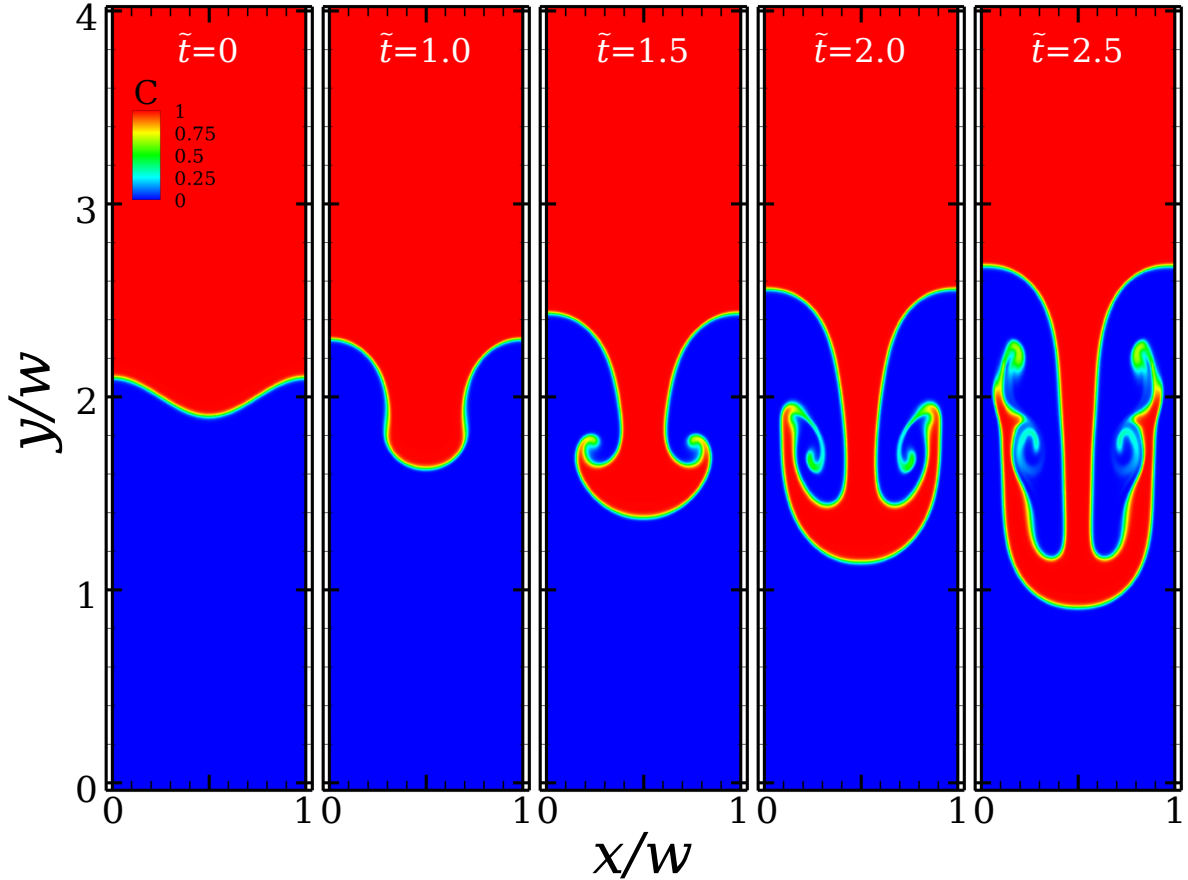

Figure 10: Contour-plots of the concentration at different dimensionless times for the Rayleigh-Taylor instability of Newtonian fluids when $At = 0.5$, ($\lambda_\eta = 1$, $Re = 3000$).

12

Later, Guermond and Quartapelle [62] considered a viscid and incompressible, Newtonian, two-phase system with variable density and found good agreement with the results of Tryggvason [60] at the same Reynolds numbers. Thus, it was demonstrated that momentum diffusion is negligible for this problem at those conditions. Ding et al. [27] and Chiu and Lin [63], performed similar investigations for $At = 0.5$ using the PF method and they also reported good agreement with the previous studies.

In this section, we examine the cases of $At = 0.5$ and $At \simeq 1$ at the approximately inviscid limit starting with the cases of Newtonian fluids and compare our results with Ding et al. [27] and Baker et al. [61] respectively. For the case of $At = 0.5$ the density ratio is set as $\lambda_\rho = \rho_1/\rho_2 = 3$, while for $At \simeq 1$, $\lambda_\rho = 300$ (which is large enough to yield less than 1% error in the Atwood number). Starting with the NN case at $At = 0.5$, the Reynolds number is fixed at $Re = 3000$ similar to the value used by Ding et al. [27]. As shown in Fig. 10, the domain is rectangular with symmetry conditions applied at the vertical sides, and wall boundary conditions at the north and south sides. All previous studies about the problem of Rayleigh-Taylor instability, report their results using a dimensionless time $\tilde{t} = t \sqrt{Atg/w}$. In order to compare our results with these studies the same time scale is adopted. At time $\tilde{t} = 0$, the initial state of the interface is described by a perturbation applied at the concentration field as

$$C(\tilde{x}, \tilde{y}, 0) = 0.5 + 0.5 \tanh\left(\frac{\tilde{y} - \tilde{y}_{in} - 0.1 \cos(2\pi\tilde{x})}{2\sqrt{2}\epsilon}\right). \quad (37)$$

All parameters with a "tilde" in the equation above indicate normalised variables with the width w of the domain. In particular, $\tilde{y}_{in} = y_{in}/w$, is defined as the initial desired position for the 0.5-contour as if there was no perturbation, and is set at $y_{in}/w = 2$.

Figure 10 displays the evolution of the Rayleigh-Taylor instability at different dimensionless times when $At = 0.5$. The contour patterns at each time-frame compare qualitatively well with previous studies [15, 27, 62, 63]. Initially the heavier fluid falls downwards forming a "spike" or finger and the lighter fluid rises forming bubble-like fronts. At $\tilde{t} = 1.5$, the heavier falling fluid has already started to roll upwards, as expected for this case of Atwood number. At later times, these "roll-ups" evolve symmetrically and keep rising upwards generating new pairs of instabilities. At the same time the front of the heavier fluid keeps moving downwards generating a characteristic thin filament. The fact that the new pairs of instabilities appear symmetrically on the left and right side of the thin filament of the falling fluid after $\tilde{t} = 1.5$, indicates the good performance of the numerical implementation. Moreover, Fig. 11 illustrates the evolution the interface positions of the 0.5-contour,
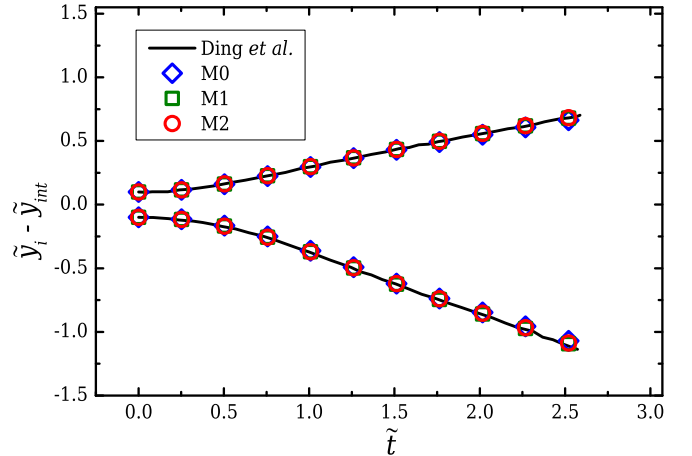

Figure 11: Front positions for the lighter and heavier fluids at different dimensionless times, for the Rayleigh-Taylor instability when $At = 0.5$ for all numerical meshes considered (cf. Table 2), compared with the solution from Ding et al. [27].

in terms of the top y-position of the rising lighter fluid and the lower y-position of the falling heavy fluid. The results are compared with the numerical study performed by Ding et al. [27] and clearly a very good quantitative agreement exists between the two studies. The grid-dependency of the numerical solution was examined using three different uniform meshes (details given in Table 2), with the results obtained for each case juxtaposed in Fig. 11. The agreement between them is very good and the solution obtained is mesh independent.

For larger At ($\rho_1 \sim 300\rho_2$), the flow patterns differ from the previous case of moderate Atwood numbers ($At = 0.5$). Figure 12 presents the evolution of the pattern for the NN case at $At \simeq 1$, considering $\lambda_\rho = 300$, $\lambda_\eta = 1$ and as previously $Re = 3000$. In contrast with the previous case of $At = 0.5$, when $At \simeq 1$ no vortices are generated. As the heavier fluid is falling downwards only a narrow spike is formed, similar to what is observed in Baker et al. [61] and Tryggvason [60]. On the other hand the lighter fluid is rising in a similar way as in the case of $At = 0.5$. In Fig. 13, the positions of the fronts of the two fluids for all numerical meshes considered are reported and are compared with the expected behaviour from Baker et al. [61]. The same behaviour where no side instabilities occur for the approximately inviscid cases investigated at a limiting Atwood number ($At \rightarrow 1$), has also been reported in other studies in the literature [26, 64].

It is known that instabilities observed in Newtonian fluid flows can be significantly modified when viscoelastic fluids are

Table 2: Mesh characteristics for the Rayleigh-Taylor instability study.

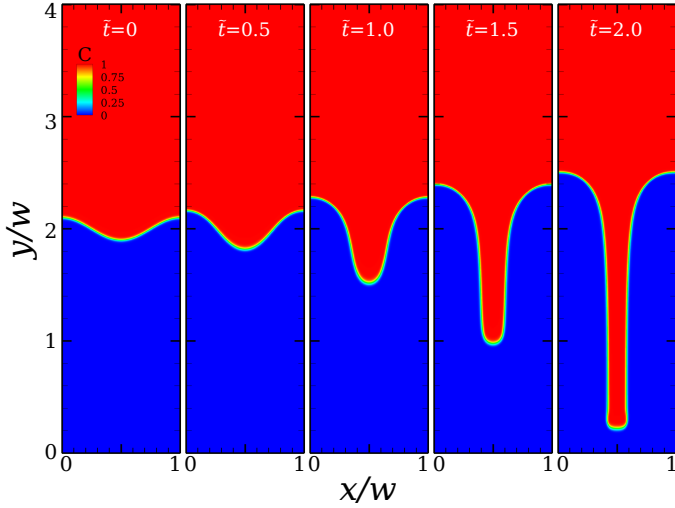| Mesh	$\delta x_{min}/w = \delta y_{min}/w$	$Cn = \epsilon/w$	ϵ/h	#Cells
M0	0.0156	0.0094	0.60	20,096
M1	0.0078	0.0047	0.60	65,536
M2	0.0050	0.0030	0.60	160,000

Figure 12: Contour-plots of the concentration at different dimensionless times for the Rayleigh-Taylor instability of Newtonian fluids when $At = 1$, ($\lambda_\eta = 1$, $Re = 3000$).
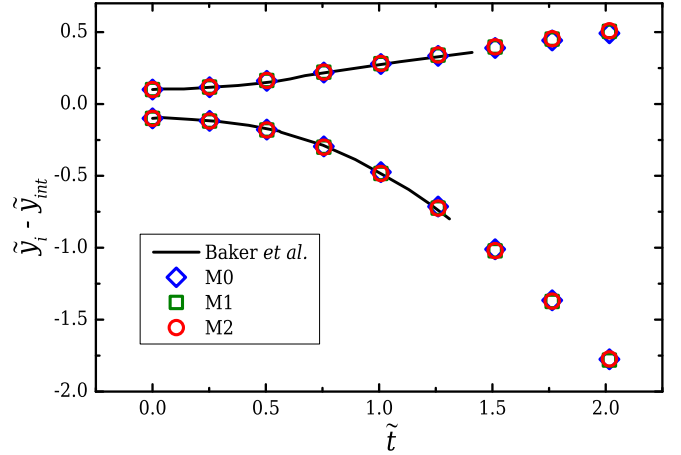

Figure 13: Front positions for the lighter and heavier fluids at different dimensionless times, for the Rayleigh-Taylor instability when $At = 1$ for all numerical meshes considered (cf. Table 2)

considered instead [65, 66]. To our knowledge, solutions of the Rayleigh-Taylor instability when viscoelastic fluids are considered have not been extensively reported in the literature. In the recent study of Boffetta *et al.* [59] the authors performed a linear stability analysis considering a small perturbation at the interface separating the two fluids and suggested that the resulting instability will grow faster for a system of viscoelastic fluids. Here, we investigate the case of $At = 0.5$ for the UCM-UCM (UU) system at $Wi = 20$ and at the same Reynolds number with the NN case discussed before ($Re = 3000$). Figure 14 illustrates the solutions obtained at different dimensionless times, where at a first instance some differences at the patterns can be seen when $\tilde{t} > 1$. In particular at $\tilde{t} = 1.5$ a small swelling is formed at the "neck" of the falling fluid while a side instability occurs at the front of the rising light fluid. Moreover, it can be seen that the roll-ups encountered at the NN case at the same time also appear here, but are slightly more enhanced. In terms of the fronts locations, Fig. 15 demonstrates the evaluated absolute positions for that of the lighter (L) and the heavier (H) fluids. The results are plotted against the equivalent response of the Newtonian fluids described in Fig. 11. Interestingly it can be seen that the UU system of viscoelastic fluids behaves like the Newtonian, with the fronts locations demonstrating negligible differences. This result is in agreement with Boffetta *et al.* [59] and their linear stability analysis. Considering that the Elasticity number, defined as $El = Wi/Re = \lambda\eta/(\rho_1 w^2)$, is very small for this particular case, can explain the small differences between the UU and NN behaviours. It worth mentioning that the value of the normalised density-weighted average viscosity (see Eq. (34)) is $\nu/(gw^3)^{1/2} = 0.0005$, additionally indicating that viscous contributions are very small.

4.2.2. Viscous regime

In this section we investigate the Rayleigh-Taylor instability for Newtonian and viscoelastic fluids at $At = 0.5$ when viscous contributions are not negligible, but on the contrary influence

the system. In the previous section the approximately inviscid limit was examined, where the Reynolds number was fixed at $Re = 3000$. Here two cases for both the NN and the UU systems are considered with $Re = 30$ and $Re = 3$. For the UU two-phase system the Weissenberg number is fixed as before at $Wi = 20$ and thus, the elasticity is gradually increased ($El = 0.67$ and $El = 6.7$).

In Fig. 16 the solutions obtained for the NN and UU systems when $Re = 30$ ($El = 0.67$ with $\nu/(gw^3)^{1/2} = 0.05$) are shown. The top row contains the contour-plots of the concentration at different dimensionless times for the NN case, while the bottom row demonstrates the equivalent response of the viscoelastic fluids at $Wi = 20$. In contrast with the previous case of the approximately inviscid limit, now clear differences occur both in the development of the instability but also with the resulting patterns. It can be seen that for the NN system up to $\tilde{t} = 2.0$ no side instabilities or mushroom formations occur, with the heavy fluid slowly falling inside the rising fluid. On the contrary for the UU case it can be seen that the heavy fluid falls faster than the equivalent Newtonian, generating a thin filament and a mushroom. This behaviour can be further realised by the evaluation of the fronts shown in Fig. 17. The instability for the UU system clearly develops faster than the equivalent for the NN. Another interesting behaviour is that up to a dimensionless time $\tilde{t} = 2.0$ the fronts of the NN system are advancing almost similarly whereas for the UU system a non-linear response occurs.

Further increasing the elasticity of the system to $El = 6.67$ by reducing the Reynolds number ($Re = 3$; $\nu/(gw^3)^{1/2} = 0.5$), even greater differences occur between the two systems considered. In Fig. 18, the solutions of the concentration obtained for the NN and UU systems are shown. It can be seen that the instability for the NN system (top row) develops very slowly, both compared to the equivalent UU case, but also compared to the other NN systems discussed before. For this case, the viscous forces become more important and manage to decelerate the system by acting opposite to gravitational forces. On the other
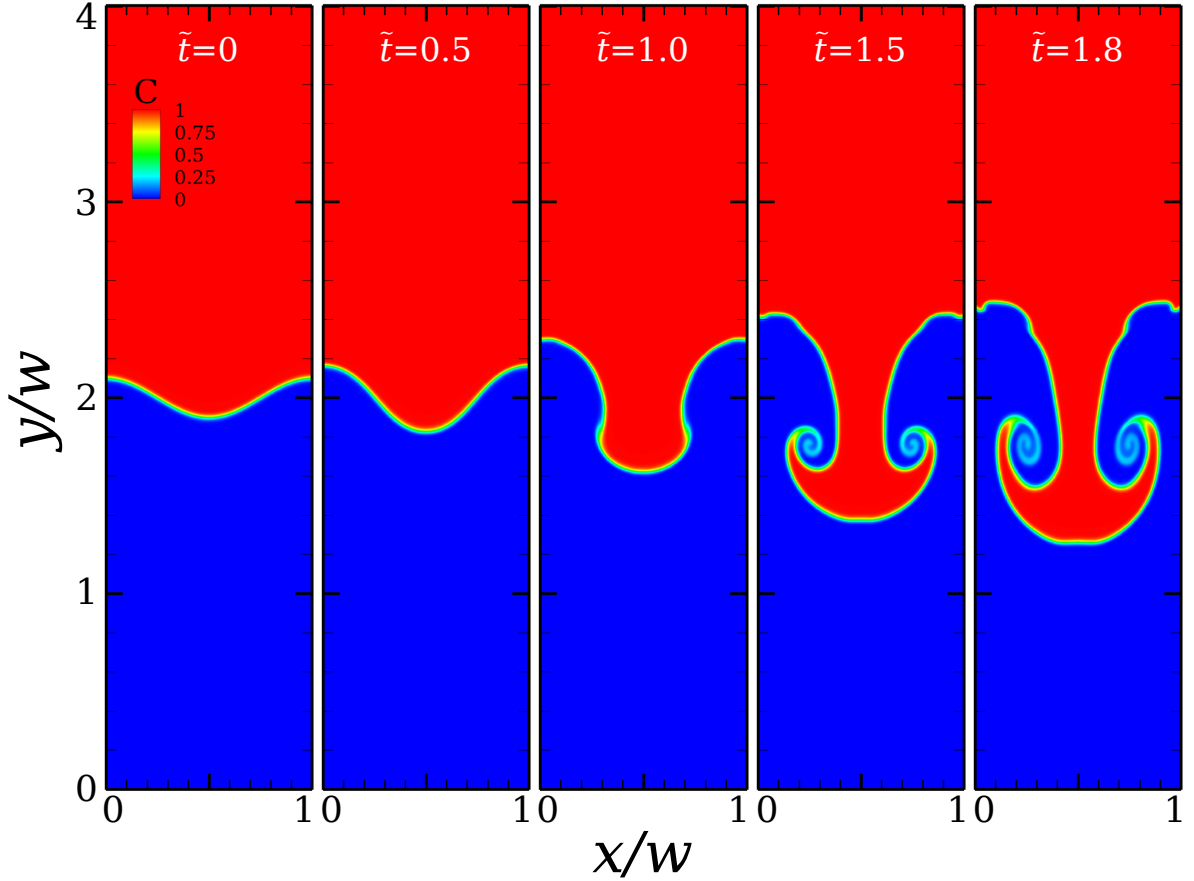
Figure 14: Contour-plots of the concentration at different dimensionless times for the Rayleigh-Taylor instability of the UCM-UCM case for $\lambda_\eta = 1$, $\lambda_\lambda = 1$ when $At = 0.5$, $Re = 3000$ and $Wi = 20$.

hand, the evolution of the UU system shown at the bottom set of the concentration contour-plots in Fig. 18 is much faster, with the presence of elasticity clearly affecting the development of the instability. The differences in the evolution of the instability
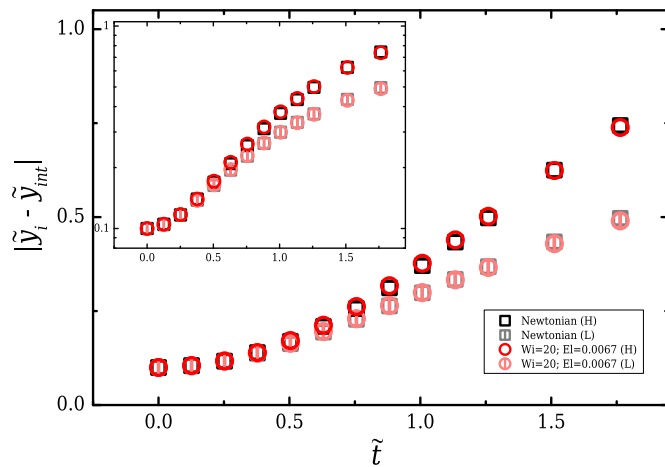

Figure 15: Absolute positions at different dimensionless times of the fronts of the heavier (H) and lighter (L) fluids when $At = 0.5$ and $Re = 3000$ ($\nu/(gw^3)^{1/2} = 0.0005$), for the UCM-UCM (UU) system with $\lambda_\lambda = 1$ at $Wi = 20$, in comparison with the equivalent locations of the Newtonian (NN) system.

are also shown in Fig. 19, where the locations of the fronts are reported as it was done for all cases so far. Clearly the two cases significantly vary in terms of developments, where additionally the presence of elastic forces is responsible for the contrast in between the fronts locations of the heavy and light fluids. This is not present in the NN system, for which the fronts evolve similarly up to the dimensionless time investigated.

The behaviours predicted here in the viscous regime are broadly in line with the predictions of Boffetta *et al.* [59], indicating that when the viscous forces start to be relatively important, clear deviations from the Newtonian behaviour occur. Concluding, for all the UU cases presented a discussion regarding the dependency of the numerical solutions upon the employed numerical meshes can be found in Appendix B.

5. Conclusions

The implementation of a two-phase solver appropriate for investigating two-phase viscoelastic fluid flows was presented here. The solver adopts the Phase Field method and is built on top of an in-house single-phase solver [16]. The discretisation of the convective Cahn-Hilliard equation, which adds the elements related to the second phase, was presented and several test-cases were examined for validation purposes. The examined cases
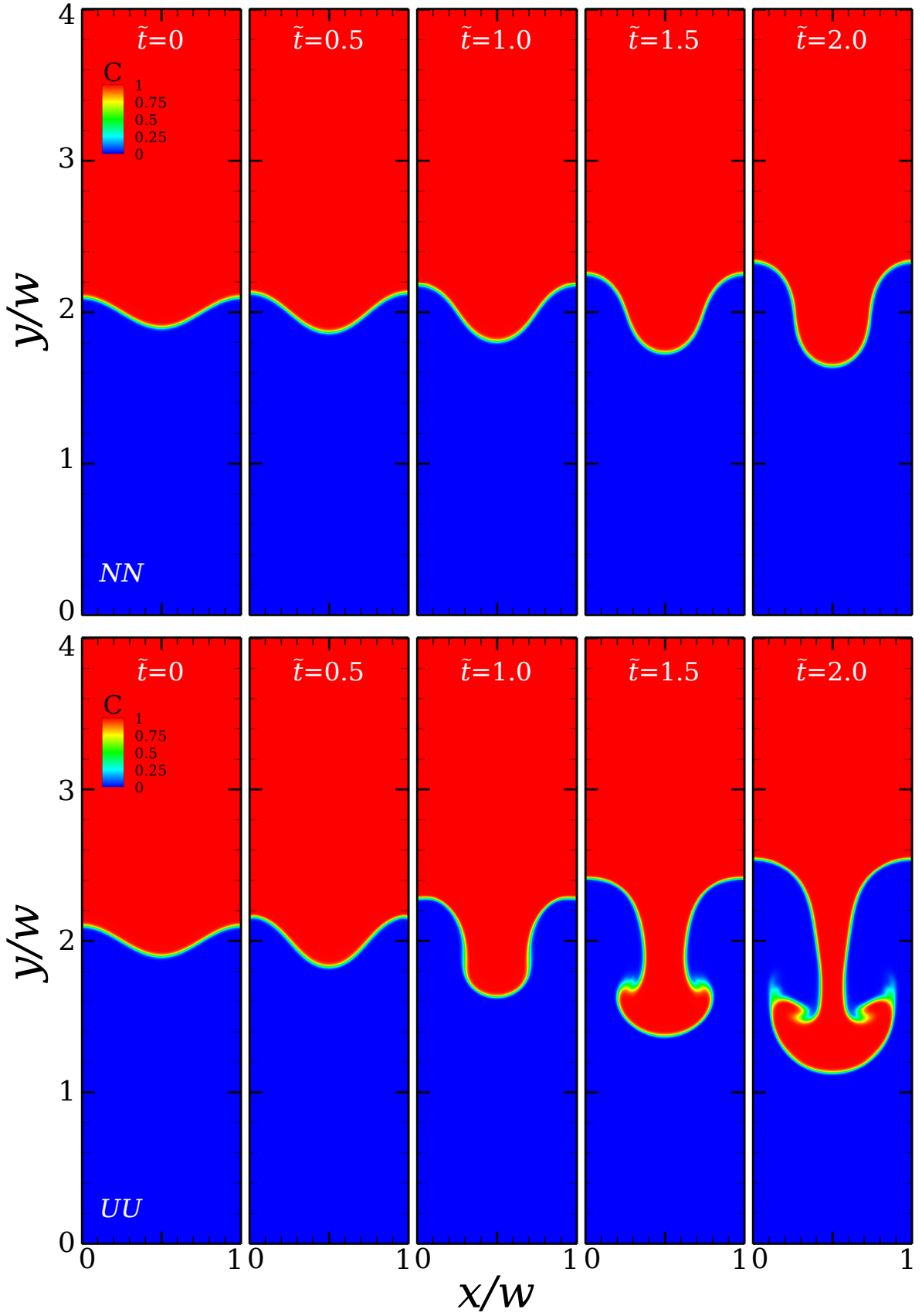
Figure 16: Contour-plots of the concentration at different dimensionless times for the Rayleigh-Taylor instability when $At = 0.5$, $\lambda_\eta = 1$ and $Re = 30$ for the Newtonian system (NN; top row) and the UCM-UCM system (UU; bottom row) with $\lambda_\lambda = 1$ at $Wi = 20$.
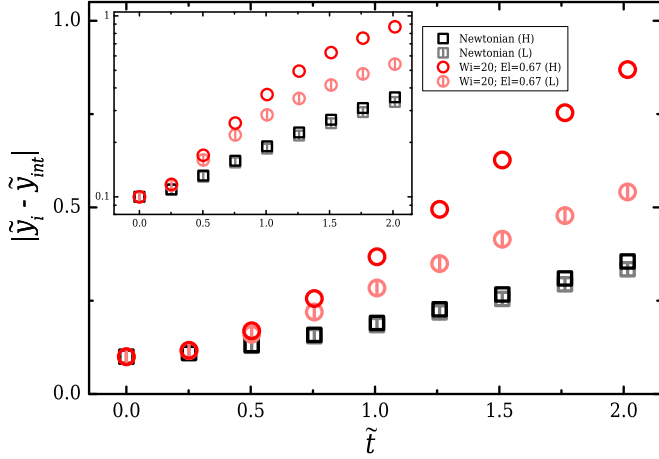
Figure 17: Absolute positions at different dimensionless times of the fronts of the heavier (H) and lighter (L) fluids when $At = 0.5$ and $Re = 30$ ($\nu/(gw^3)^{1/2} = 0.05$), for the UCM-UCM (UU) system with $\lambda_\lambda = 1$ at $Wi = 20$, in comparison with the equivalent locations of the Newtonian (NN) system.

where distinguished based on the value of the interfacial tension coefficient.

When $\sigma \neq 0$, the diffusion term in CH and the surface forces in the momentum equation are both accounted for. The capability of the numerical implementation to accurately predict the expected behaviour was tested by investigating the oscillation of a square drop and the deformation of a drop under constant shear. Overall the solver performs satisfactory, illustrating adequate capturing of the expected physics. Initially, for the case of the oscillating droplet the square-shaped droplet was successfully driven to an equilibrium state, obtaining a final circular shape. During the intermediate stages the drop obtained several shapes, acquiring an oscillatory movement. At the final state where the oscillations ceased, the evaluated pressure difference along the interface of the two fluids was found to be in agreement with the pressure drop expected from the Young-Laplace formula. The second test-case conducted, examined the droplet deformation under constant shear for NN, NV, VN and VV systems. The results of the deformed interface of the drop of each system demonstrated that the two-phase solver predicts the same behaviour as Chinyoka *et al.* [54]. It was also found that by introducing elasticity in one of the phases of the NN case, the applied deformation will be reduced.

When the interfacial tension coefficient is set to zero ($\sigma = 0$) the Rayleigh-Taylor instability for Newtonian and viscoelastic fluids was examined. Two regimes where identified: the approximately inviscid and the viscous. The two-phase solver was initially validated in the former regime for different Atwood numbers ($At = 0.5$ and $At \simeq 1$), capturing well the Rayleigh-Taylor instability patterns and the fronts locations for the NN systems. Then, in the same regime and for $At = 0.5$, the case of the UU system was investigated for $Wi = 20$ demonstrating a similar response with the NN system in terms of the instability development. For the viscous regime, solutions of the Rayleigh-Taylor instability were provided for $At = 0.5$. Initially large differences in the behaviour of the NN systems compared to the response encountered in the approximately inviscid regime at the same Atwood number were reported, demonstrating the important role of viscous forces and their effects against gravity forces. For the viscoelastic cases considered (at $Wi = 20$), clear differences in the development of the instabilities were found between the NN and the UU systems, indicating the important role of elasticity.

The Rayleigh-Taylor instability problem is very rich, and as presented here, even for Newtonian fluids different regimes exist with various resulting behaviours. Introducing elasticity further complicates the examined problem, where different responses are expected depending on the properties of the viscoelastic fluid considered. Therefore, we intend in a future study to investigate further this problem for viscoelastic fluid flows, considering also more complex viscoelastic models than the UCM.

A. Mesh resolution for the oscillating droplet

Here we provide a comparison between the CFD results for the case of the oscillating droplet obtained using the meshes M1 (as presented in Section 4.1.1) and M2 with $Cn = \epsilon/R_{eff} = 0.008$ and $\epsilon/h = 0.60$. In particular, Fig. A.20 illustrates the behaviour of the 0.5-contour of the concentration for the meshes M1 and M2 at different dimensionless times (see Fig. 5). It can be seen that the method is not very sensitive to grid refinement and to small changes that occur to the curvature of the corners with respect to the mesh size .

B. Mesh resolution for the Rayleigh-Taylor instability

Here we provide a comparison between the CFD results for the viscoelastic fluids obtained using meshes M1 and M2 (details in Table 2) and presented in Section 4.2. In particular, Fig. B.21 illustrates the behaviour of the 0.5-contour of the concentration for the meshes M1 and M2 when the UU systems are considered, which is used for evaluating the locations of the fronts in all the cases discussed in Section 4.2. The top-row corresponds to the case with $Wi = 20$, $Re = 3000$ ($El = 0.0067$), the middle row to $Wi = 20$, $Re = 30$ ($El = 0.67$) and the bottom row to the more elastic case at $Wi = 20$, $Re = 3$ ($El = 6.7$). For all cases a nice agreement is found, demonstrating the independence of the numerical solution. It is mentioned that only at late times small deviations are observed between the meshes as a consequence of the increased resolution of the interface and the reduction of numerical diffusion for the more refined mesh.

Supplementary Material

Video demonstrating the oscillations of the initially square Newtonian drop inside the Newtonian matrix fluid.
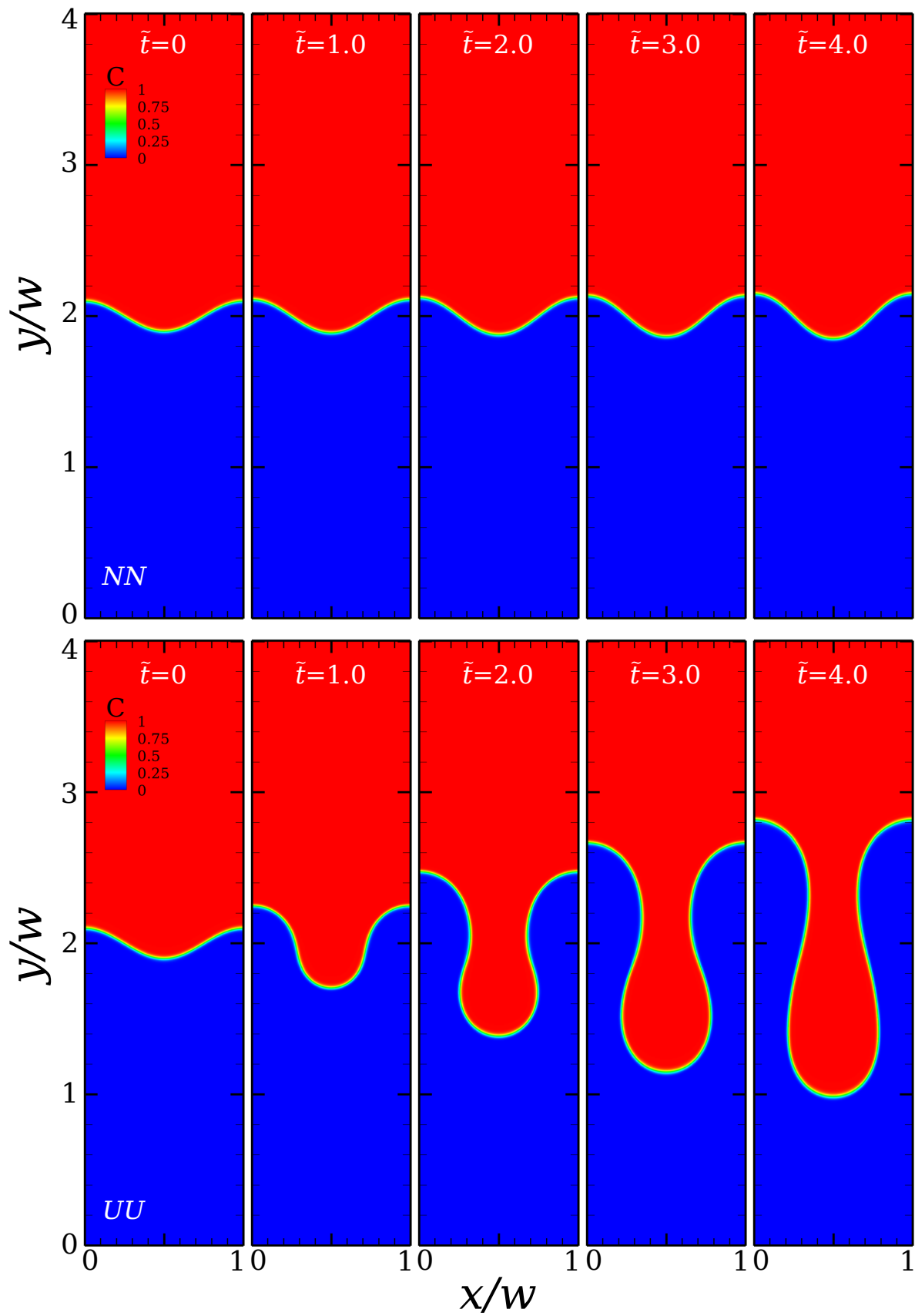
Acknowledgements

Figure 18: Contour-plots of the concentration at different dimensionless times for the Rayleigh-Taylor instability when $At = 0.5$, $\lambda_\eta = 1$ and $Re = 3$ for the Newtonian system (NN; top row) and the UCM-UCM system (UU; bottom row) with $\lambda_\lambda = 1$ at $Wi = 20$.
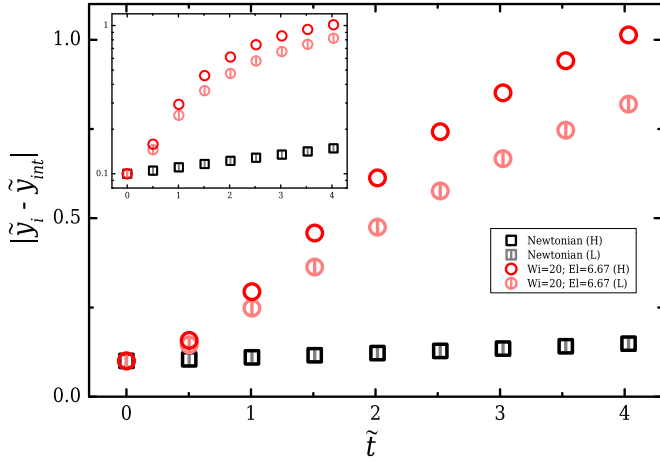
Figure 19: Absolute positions at different dimensionless times of the fronts of the heavier (H) and lighter (L) fluids when $At = 0.5$ and $Re = 3$ ($\nu/(gw^3)^{1/2} = 0.5$), for the UCM-UCM (UU) system with $\lambda_\lambda = 1$ at $Wi = 20$, in comparison with the equivalent locations of the Newtonian (NN) system.
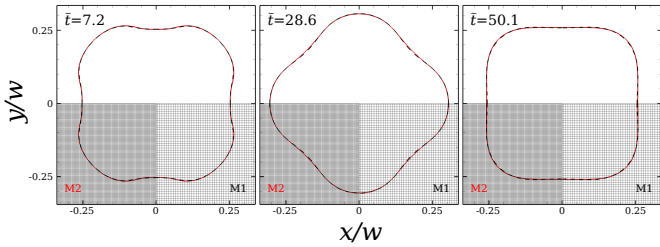

Figure A.20: Behaviour of the 0.5-contour at different dimensionless times. The bottom left and bottom right of each figure illustrate the meshes M2 and M1 respectively.

and discussions during the implementation procedure. K. Z. and R. J. P. acknowledge funding from the EPSRC (UK) through Grant No. EP/M025187/1.

References

[1] T. Tezduyar, Interface-tracking and interface-capturing techniques for finite element computation of moving boundaries and interfaces, Comput. Method Appl. M. 195 (2006) 29833000. doi:10.1016/j.cma.2004.09.018.

[2] Y. Zhang, H. Liu, Microdroplet technology: principles and emerging applications in biology and chemistry, Springer New York, (2012), Ch. Physics of Multiphase Microflows and Microdroplets, pp. 1–21. doi:10.1007/978-1-4614-3265-4.

[3] G. Tryggvason, B. Bunner, A. Esmaeeli, D. Juric, N. Al-Rawahi, W. Tauber, J. Han, S. Nas, Y. J. Jan, A front-tracking method for the computations of multiphase flow, J. Comput. Phys. 169 (2001) 708–759. doi:10.1006/jcph.2001.6726.

[4] C. S. Peskin, The fluid dynamics of heart valves: Experimental, theoretical, and computational methods, Annu. Rev. Fluid Mechanics 14 (1982) 235. doi:10.1146/annurev.fl.14.010182.001315.

[5] R. Mittal, G. Iaccarino, Immersed boundary methods, Annu. Rev. Fluid Mechanics 37 (2005) 239–261. doi:10.1146/annurev.fluid.37.061903.175743.

[6] T. Y. Hou, J. S. Lowengrub, M. J. Shelley, Boundary integral methods for multicomponent fluids and multiphase materials, J. Comput. Phys. 169 (2001) 302–362. doi:10.1006/jcph.2000.6626.

[7] D. Jacqmin, Calculation of Two-Phase Navier-Stokes Flows Using Phase-Field Modeling, J. Comput. Phys. 155 (1999) 96–127. doi:10.1006/jcph.1999.6332.
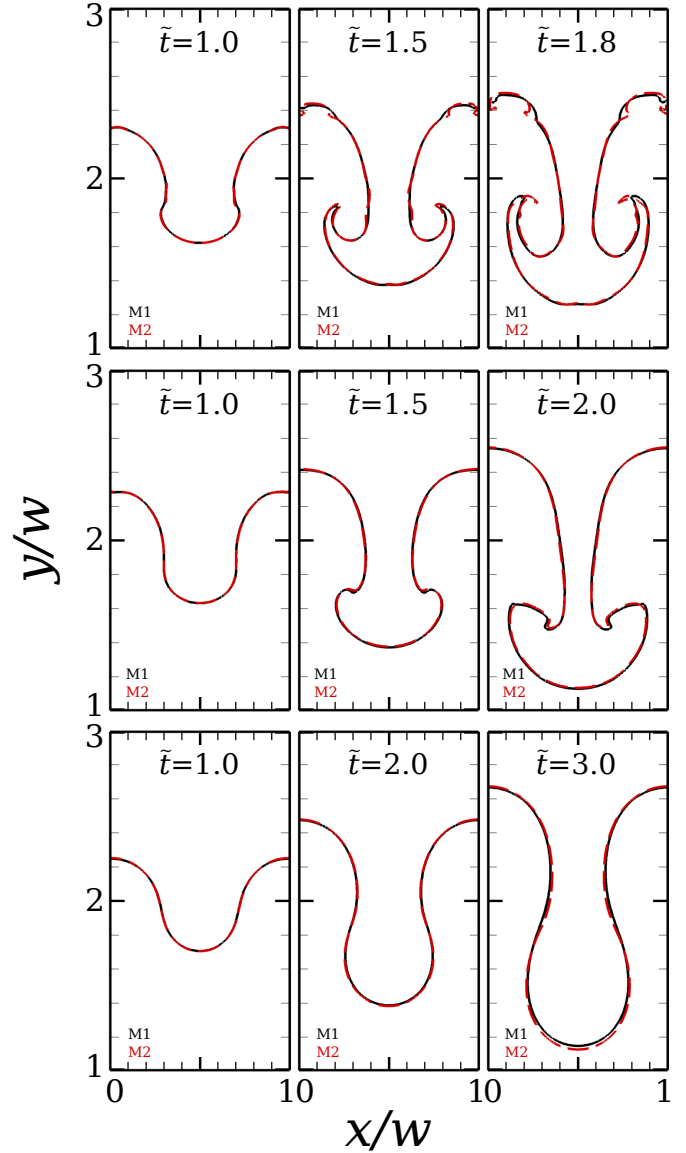
Figure B.21: Behaviour of the 0.5-contour from which the locations of the fronts are evaluated for the all the UU cases considered and discussed in Section 4.2. Top row corresponds to $Wi = 20$, $Re = 3000$, middle row to $Wi = 20$, $Re = 30$ and bottom row to $Wi = 20$, $Re = 3$.

[8] P. Yue, J. J. Feng, C. Liu, J. Shen, A diffuse-interface method for simulating two-phase flows of complex fluids, J. Fluid Mech. 515 (2004) 293–317. doi:10.1017/S0022112004000370.

[9] F. Magaletti, F. Picano, M. Chinappi, L. Marino, C. M. Casciola, The sharp-interface limit of the Cahn-Hilliard/Navier-Stokes model for binary fluids, J. Fluid Mech. 714 (2013) 95–126. doi:10.1017/jfm.2012.461.

[10] C. W. Hirt, D. B. Nichols, Volume of fluid (VOF) method for the dynamics of free boundaries, J. Comput. Phys. 39 (1981) 201–225. doi:10.1016/0021-9991(81)90145-5.

[11] R. A. Figueiredo, C. M. Oishi, A. M. Afonso, I. V. M. Tasso, J. A. Cuminato, A two-phase solver for complex fluids: Studies of the Weissenberg effect, Int. J. Multiphas. Flow 84 (2016) 98–115. doi:10.1016/j.ijmultiphaseflow.2016.04.014.

[12] J. A. Sethian, P. Semerka, Level set methods for fluid interfaces, Annu. Rev. Fluid Mechanics 35 (2003) 341–372. doi:10.1146/annurev.fluid.35.101101.161105.

[13] M. Sussman, P. Smereka, S. Osher, A level set approach for computing

solutions to incompressible two-phase flows, J. Comput. Phys. 114 (1994) 146–159. `doi:10.1006/jcph.1994.1155`.

[14] D. M. Anderson, G. B. McFadden, A. A. Wheeler, Diffuse-interface methods in fluid mechanics, Annu. Rev. Fluid Mechanics 30 (1998) 139–165. `doi:10.1146/annurev.fluid.30.1.139`.

[15] J. Kim, Phase-Field Models for Multi-Component Fluid Flows, Comput. Method Appl. M. 12 (2012) 613–661. `doi:10.4208/cicp.301110.040811a`.

[16] P. J. Oliveira, F. T. Pinho, G. A. Pinto, Numerical simulation of non-linear elastic flows with a general collocated finite-volume method, J. Non-Newton. Fluid Mech. 79 (1998) 1–43. `doi:10.1016/S0377-0257(98)00082-2`.

[17] J. D. Van der Waals, The thermodynamic theory of capillarity flow under the hypothesis of a continuous variation of density. English translation by J. S. Rowlinson, J. Stat. Phys 20 (1979) 197–244. `doi:10.1007/BF01011514`.

[18] J. Gibbs, On the equilibrium of heterogeneous substances, Trans. Conn. Acad. Sci. III (1875) 108–248.

[19] J. W. Cahn, J. E. Hilliard, Free Energy of a Nonuniform System. 1. Interfacial Free Energy, J. Chem. Phys. 28 (1958) 258–267. `doi:10.1063/1.1744102`.

[20] J. W. Cahn, J. E. Hilliard, Free Energy of a Nonuniform System. 3 Nucleation in a two-component incompressible fluid, J. Chem. Phys. 31 (1959) 688–699. `doi:10.1063/1.1730447`.

[21] P. C. Hohenberg, B. I. Halperin, Theory of dynamic critical phenomena, Rev. Mod. Phys. 49 (1977) 435–479. `doi:10.1103/RevModPhys.49.435`.

[22] Y. Sun, C. Beckermann, Sharp interface tracking using the phase-field equation, J. Comput. Phys. 220 (2007) 626–653. `doi:10.1016/j.jcp.2006.05.025`.

[23] L. K. Antanovskii, A phase field model of capillarity, Phys. Fluids. 7 (1995) 747–753. `doi:10.1063/1.868598`.

[24] V. E. Badalassi, H. D. Ceniceros, S. Banerjee, Computation of multiphase systems with phase field models, J. Comput. Phys. 190 (2003) 371–397. `doi:10.1016/S0021-9991(03)00280-8`.

[25] J. Kim, A continuous surface tension force formulation for diffuse-interface models, J. Comput. Phys. 204 (2005) 784–804. `doi:10.1016/j.jcp.2004.10.032`.

[26] S. A. Nabavizadeh, M. Eshraghi, S. D. Felicelli, S. N. Tewari, R. N. Grugel, Effect of bubble-induced marangoni convection on dendritic solidification, Int. J. Multiphas. Flow 116 (2019) 137–152. `doi:https://doi.org/10.1016/j.ijmultiphaseflow.2019.04.018`.

[27] H. Ding, P. D. M. Spelt, C. Shu, Diffuse interface model for incompressible two-phase flows with large density ratios, J. Comput. Phys. 226 (2007) 2078–2095. `doi:10.1016/j.jcp.2007.06.028`.

[28] H. A. Akhlaghi Amiri, A. A. Hamouda, Evaluation of level set and phase field methods in modeling two phase flow with viscosity contrast through dual-permeability porous medium, Int. J. Multiphas Flow 52 (2013) 22–34. `doi:https://doi.org/10.1016/j.ijmultiphaseflow.2012.12.006`.

[29] D. Borzacchiello, E. Leriche, B. Blottiére, J. Guillet, Three-dimensional finite volume computation of viscoelastic fluid encapsulation by phase-field modeling, J. Non-Newton. Fluid Mech. 200 (2013) 52–64. `doi:http://dx.doi.org/10.1016/j.jnnfm.2012.11.003`.

[30] E. J. Hemingway, H. Kusumaatmaja, S. M. Fielding, Edge fracture in complex fluids, Phys. Rev. Lett. 119 (028006). `doi:10.1103/PhysRevLett.119.028006`.

[31] E. J. Hemingway, S. M. Fielding, Edge fracture instability in sheared complex fluids: onset criterion and possiblemitigation strategy, J, Rheol. 63 (2019) 735–750. `doi:10.1122/1.5095717`.

[32] A. A. Donaldson, D. M. Kirpalani, A. Macchi, Diffuse interface tracking of immiscible fluids: Improving phase continuity through free energy density selection, Int. J. Multiphase Flow 37 (2011) 777–787. `doi:10.1016/j.ijmultiphaseflow.2011.02.002`.

[33] Y. Oono, S. Puri, Study of phase-separation dynamics by use of cell dynamical systems. I. Modeling, Phys. Rev. A. 38 (1988) 434–453. `doi:10.1103/physreva.38.434`.

[34] R. H. Nochetto, M. Paolini, C. Verdi, A dynamic mesh algorithm for curvature dependent evolving interfaces, J. Comput. Phys. 123 (1996) 296–310. `doi:10.1006/jcph.1996.0025`.

[35] O. Wodo, B. Ganapathysubramanian, Computationally efficient solution to the Cahn-Hilliard equation: Adaptive implicit time schemes, mesh sensitivity analysis and the 3D isoperimetric problem, J. Comput. Phys. 230 (2011) 6037–6060. `doi:10.1016/j.jcp.2011.04.012`.

[36] M. De Menech, P. Garstecki, F. Jousse, H. A. Stone, Transition from squeezing to dripping in a microfluidic t-shaped junction, J. Fluid Mech. 595 (2008) 141–161. `doi:10.1017/S002211200700910X`.

[37] P. Yue, C. Zhou, J. J. Feng, Sharp-interface limit of the CahnHilliard model for moving contact lines, J. Fluid Mech. 645 (2010) 279–294.

[38] K. Zografos, Intelligent design of microfluidic components for newtonian and complex fluid systems, Ph.D. thesis, Department of Mechanical and Aerospace Engineering, Strathclyde University (2017). URL `https://ethos.bl.uk/OrderDetails.do?uin=uk.bl.ethos.714732`

[39] A. Komrakova, O. Shardt, D. Eskin, J. Derksen, Lattice Boltzmann simulations of drop deformation and breakup in shear flow, Int. J. Multiphase Flow 126 (2014) 150–159.

[40] M. Gurtin, D. Polignone, J. Vinals, Two-phase binary fluids and immiscible fluids described by an order parameter, Math. Mod. Meth. Appl. S. 6 (1996) 815–831. `doi:10.1142/S0218202596000341`.

[41] D. Jacqmin, Contact-line dynamics of a diffuse fluid interface, J. Fluid Mech. 402 (2000) 57–88. `doi:10.1017/S0022112099006874`.

[42] V. V. Khatavkar, P. D. Anderson, P. C. Duineveld, H. E. H. Meijer, Diffuse-interface modelling of droplet impact, J. Fluid Mech. 581 (2007) 97–127. `doi:10.1017/S002211200700554X`.

[43] P. W. Bates, P. C. Fife, The Dynamics of Nucleation for the Cahn-Hilliard Equation, SIAM J. Appl. Math. 53 (1993) 990–1008. URL `https://www.jstor.org/stable/2102259?seq=1`

[44] J. G. Oldroyd, On the formulation of eequation of state, Proc. R. Soc. Lond. Ser-A 200 (1950) 523–541. `doi:10.1098/rspa.1950.0035`.

[45] P. J. Oliveira, F. T. Pinho, Numerical procedure for the computation of fluid flow with arbitrary stress-strain relationship, Numer. Heat Tr. B-Fund. 35 (1999) 295–315. `doi:10.1080/104077999275884`.

[46] M. A. Alves, P. J. Oliveira, F. T. Pinho, A convergent and universally bounded interpolation scheme for the treatment of advection, Int. J. Numer. Meth. Fluids 41 (2003) 47–75. `doi:10.1002/fld.428`.

[47] J. H. Ferzinger, M. Perić, Computational Methods for Fluid Dynamics, Springer Berlin Heidelberg, 2002. `doi:10.1007/978-3-642-56026-2`.

[48] P. Yue, C. Zhou, J. J. Feng, Spontaneous shrinkage of drops and mass conservation in phase-field simulations, J. Comput. Phys. 223 (2007) 1–9. `doi:10.1016/j.jcp.2006.11.020`.

[49] M. Peric, A finite volume method for the prediction of three-dimensional fluid flow in complex ducts, Ph.D. thesis, Imperial Colege, University of London (1985). URL `http://hdl.handle.net/10044/1/7601`

[50] J. U. Brackbill, D. B. Kothe, C. Zemach, A continuum method for modeling surface tension, J. Comput. Phys. 100 (1992) 335–354. `doi:10.1016/0021-9991(92)90240-Y`.

[51] G. H. McKinley, Dimensionless groups for understanding free surface flows of complex fluids, Society of Rheology, Rheology Bulletin 74 (2005) 6–9. URL `http://hdl.handle.net/1721.1/18086`

[52] M. Zhang, Simulation of surface tension method in 2D and 3D with smoothed particle hydrodynamics method, J. Comput. Phys. 229 (2010) 7238–7259. `doi:10.1016/j.jcp.2010.06.010`.

[53] G. I. Taylor, The formation of emulsions in definable fields of flow, Proc. R. Soc. London, Ser. A 146 (1934) 501–523. `doi:10.1098/rspa.1934.0169`.

[54] T. Chinyoka, Y. Y. Renardy, M. Renardy, D. B. Khismatullin, Two-dimensional study of drop deformation under simple shear for Oldroyd-B fludis, J. Non-Newton. Fluid Mech. 130 (2005) 45–56. `doi:10.1016/j.jnnfm.2005.07.005`.

[55] P. Capobianchi, F. T. Pinho, M. Lappa, M. S. N. Oliveira, Thermocapillary motion of a newtonian drop in a dilute viscoelastic fluid, J. Non-Newton. Fluid Mech. 270 (2019) 8–22. `doi:10.1016/j.jnnfm.2019.06.006`.

[56] G. I. Taylor, The instability of liquid surfaces when accelerated in a direction perpendicular to their planes, Proc. R. Soc. London Ser. A 201 (192-196). `doi:10.1098/rspa.1950.0052`.

[57] D. H. Sharp, An overview of Rayleigh-Taylor instability, Physica D 12 (1984) 3–10. `doi:10.1016/0167-2789(84)90510-4`.

[58] R. Menikoff, R. C. Mjolsness, D. H. Sharp, C. Zemach, Unstable normal

mode for Rayleigh-Taylor instability in viscous fluids, Phys Fluids 20 (1977) 2000–2004. `doi:https://doi.org/10.1063/1.861831`.

[59] G. Boffetta, A. Mazzino, S. Musacchio, L. Vozella, Rayleigh-Taylor instability in a viscoelastic binary fluid, J. Fluid. Mech. `doi:10.1017/S0022112009992497`.

[60] G. Tryggvason, Numerical simulations of the Rayleigh-Taylor instability, J. Comput. Phys. 75 (1988) 253–282. `doi:10.1016/0021-9991(88)90112-X`.

[61] G. R. Baker, D. I. Meiron, S. A. Orszag, Vortex simulations of the Rayleigh-Taylor instability, Phys. Fluids 23 (1980) 1485–1490. `doi:10.1063/1.863173`.

[62] J. L. Guermond, L. Quartapelle, A projection FEM for variable density incompressible flows, J. Comput. Phys. 165 (2000) 167–188. `doi:10.1006/jcph.2000.6609`.

[63] P. H. Chiu, Y. T. Lin, A conservative phase field method for solving incompressible two-phase flows, J. Comput. Phys. 230 (2011) 185–204. `doi:10.1016/j.jcp.2010.09.021`.

[64] J. Y. Shao, C. Shu, A hybrid phase field multiple relaxation time lattice boltzmann method for the incompressible multiphase flow with large density contrast, Int. J. Numer. Methods Fluids 77 (2015) 526–543. `doi:https://doi.org/10.1002/fld.3995`.

[65] N. Burshtein, K. Zografos, A. Q. Shen, R. J. Poole, S. J. Haward, Inertioelastic flow instability at a stagnation point, Phys. Rev. X 7 (041039). `doi:10.1103/PhysRevX.7.041039`.

[66] K. Zografos, N. Burshtein, A. Q. Shen, S. J. Haward, R. Poole, Elastic modifications of an inertial instability in a 3d cross-slot, J. Non-Newton. Fluid 262 (2018) 12–24. `doi:10.1016/j.jnnfm.2018.02.002`.